

**Close Out and Final Report for
NASA Glenn Cooperative Agreement NAG3-2601**

**Magnetic-Nozzle Studies for Fusion Propulsion Applications: Gigawatt Plasma Source
Operation and Magnetic Nozzle Analysis**

James H. Gilland/Ohio Aerospace Institute

Dr. Ioannis Mikellides/SAIC

Dr. Pavlos Mikellides/Arizona State University

Dr. Gerald Gregorek and Dr. Darin Marriott/Ohio State University

Executive Summary

This project has been a multiyear effort to assess the feasibility of a key process inherent to virtually all fusion propulsion concepts: the expansion of a fusion-grade plasma through a diverging magnetic field. Current fusion energy research touches on this process only indirectly through studies of plasma divertors designed to remove the fusion products from a reactor. This project was aimed at directly addressing propulsion system issues, without the expense of constructing a fusion reactor. Instead, the program designed, constructed, and operated a facility suitable for simulating fusion reactor grade edge plasmas, and to examine their expansion in an expanding magnetic nozzle. The approach was to create and accelerate a dense (up to 10^{20} m^{-3}) plasma, stagnate it in a converging magnetic field to convert kinetic energy to thermal energy, and examine the subsequent expansion of the hot (100's eV) plasma in a subsequent magnetic nozzle.

Throughout the project, there has been a parallel effort between theoretical and numerical design and modelling of the experiment and the experiment itself. In particular, the MACH2 code was used to design and predict the performance of the magnetoplasmadynamic (MPD) plasma accelerator, and to design and predict the design and expected behavior for the magnetic field coils that could be added later. Progress to date includes the theoretical accelerator design and construction, development of the power and vacuum systems to accommodate the powers and mass flow rates of interest to our research, operation of the accelerator and comparison to theoretical predictions, and computational analysis of future magnetic field coils and the expected performance of an integrated source-nozzle experiment.

The facility is based on the "Godzilla" pulse forming network, a 1.8 MJ capacitor bank capable of delivering its energy in 1.8 ms, delivering 1 GW to a matched load. The experiment powered by Godzilla is housed in a 16' long, 2' diameter metal vacuum chamber, evacuated to sub-millitorr pressures prior to operation. The plasma accelerator is a coaxial MPD thruster 20" in diameter. Experimental data reported herein are primarily terminal voltage and current

characteristics over a range of helium mass flow rates from 2 to 30 g/s, and some initial plasma temperature, density, and velocity measurements. The latter data were obtained using two triple probes separated axially along the axis of the chamber to determine time-of-flight of the plasma.

Calculations performed concurrently with the experiments addressed several areas of the experiment. Initial designs of the source included predictions of performance for several mass flow rates and power levels. During operation of the source, the MACH2 code was also used to analyze the mass flow system behavior and compare theory to the experimentally measured pressures measured in calibrating the accelerator. The behavior of the accelerator-generated plasma flowing from the interelectrode region of the accelerator into a representative stagnating magnetic field has also been assessed using MACH2 in order to prepare for possible future experiments in magnetic nozzle performance.

As of the conclusion of this effort, the plasma accelerator has been operated at conditions of 2 to 30 g/s of helium, and up to 300 MWe of power. Current levels reached 300 kA in the device. The accelerator data shows good agreement with established MPD thruster theory and gives us confidence to identify regimes in which the device can be used for magnetic nozzle experiments. In particular, scaling of the voltage-current characteristics with the similarity parameter $\beta = J/J_{fi}$ follows the linear-cubic behavior observed in MPD thrusters. Some preliminary density, temperature, and velocity measurements also indicate that the accelerator is suitable for high temperature plasma generation.

Concurrent modeling of the magnetic nozzle behavior using MACH2 first identified some technical issues with the baseline electrode geometry; specifically, that the flow out of the accelerator converged and choked too close to the electrodes, resulting in shocks and inefficient stagnation of the discharge, and perturbation of the accelerator discharge. The results suggested that if the bulk of the flow is re-directed further downstream from the inner electrode, unfavorable interference between the applied magnetic field and the source flow may be minimized. To remedy this, various geometrical configurations of the MPD electrodes were simulated in an attempt to re-direct the plasma flow downstream of the inner electrode. Two requirements drove the new geometrical arrangements: 1) redirect the flow enough downstream of the inner electrode so that the effect of the applied magnetic on the flow at the electrode gap is minimal; and 2) match the peak magnetic pressure from the applied magnetic field to the peak steady state plasma pressure attained using the accelerator without an applied field.

Three different arrangements were attempted. Only the arrangement that incorporated a thicker inner electrode, shaped in conical fashion (resembling the divergent section of a conical nozzle), showed promise. With this configuration and with the coil "turned off" the peak plasma pressure point at centerline was computed by MACH2 to occur ~50 cm farther downstream of the location computed in the original MPD geometry. When the magnetic field was applied after steady state flow had been attained, oscillations of the plasma pressure at the electrode were captured as a result of compression wave reflections from the downstream field. Contrary to previous cases the flow at the gap recovered the first two compression waves. The simulations with this arrangement must be prolonged to confirm that steady state may be achieved (runs were taken to 400 microseconds). At about 300 microseconds the temperature ~3 m downstream of the inner electrode was more than 40 eV and the flow mach number was mostly subsonic. The plasma pressure however was still about two orders of magnitude less than the desired value of a few atmospheres. Future simulations must attempt relatively small modifications to the present coil

in order to further compress the flow. With the present configuration more than 50% of the flow kinetic energy is predicted to be retained by the plasma far downstream of coil.

Magnetic-Nozzle Studies for Fusion Propulsion Applications : Gigawatt Plasma Source Operation and Magnetic Nozzle Analysis

1. Introduction

Because of the high plasma temperatures achievable, fusion propulsion offers the potential for high specific impulse, high power propulsion. Temperatures in neutron-free, fusion systems exceed values for "conventional" D-T fusion concepts by factors of about five (~ 100 keV vs 10-20 keV). Plasma particles from a D-He³ fusion reactor would have an average speed of 3,000 km/s. Even though these velocities are much higher than the optimum values for fast interplanetary travel, fusion reactants can still be utilized to heat a much larger mass of low-molecular-weight plasma (e.g., hydrogen) to stagnation temperatures of ~ 100 eV.

Experimental terrestrial fusion reactors remove plasma via divertors, which detach the hot plasma from the magnetic lines by neutralizing it via collisions with either a neutral gas or solid target and pumping the gas away. These systems are not intended to exhaust the plasma at high speed. Propulsive applications require the plasma to flow along magnetic field lines and detach at the proper location in the expansion. To simulate a fusion plasma exhaust, the physics can be simulated by a magnetic "cusp" configuration composed from proper placement of magnet coils as shown in Figure 1. Physically, the interaction of plasma and magnetic field (magnetic field lines of constant flux are depicted as compressed ellipses in Figure 1) in this region forms a thin layer of diamagnetic currents² that in-turn interact with the magnetic field to provide a confining Lorentz force that balances the plasma pressure-gradient forces and stagnates the flow. Because of the high degree of ionization in the plasma, only a portion of the plasma intermixes with the magnetic field, providing distinct regions of field-free plasma and plasma-free magnetic field. These azimuthal currents are a consequence of the density gradient inside the layer, which results in non-zero Larmor gyration average velocities, (diamagnetic drift). The same principles are utilized to subsequently expand the propellant through the subsequent diverging main magnetic nozzle and thus provide the optimum speeds.

The stagnation and expansion of high-temperature conductive plasma in a magnetic field has not been demonstrated experimentally for plasmas relevant to fusion propulsion. An experimental investigation into this process is ongoing at Ohio State University, simulating a fusion exhaust plasma using a multimegawatt MPD thruster firing into an appropriate magnetic field configuration. The full research effort has consisted of parallel experimental and theoretical research. The theory and numerical modeling has been used to design and predict the experimental system, as well as to assist in the data analysis. Progress up to the end of this contract led to design, construction and operation of the plasma source and initial measurements of its performance, as well as computational assessment of the source mass flow system and design of the magnetic coils necessary to simulate a fusion nozzle expansion.

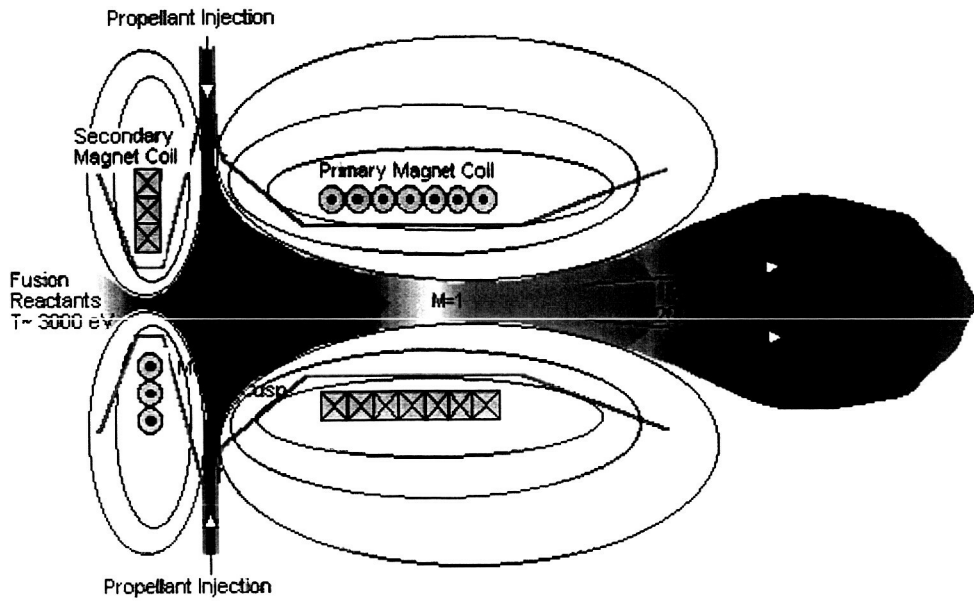


Figure 1-1. Schematic of the fusion propulsion concept depicting fusion-reactant mixing with injected cold propellant and magnetically-guided plasma flow.

2. Experimental Results

2.1. Facility

The experiment consists primarily of “Godzilla”, a GW-level LC-ladder energy source¹ and an inverse-pinch switching system already modified into an MPD plasma source.² Godzilla is made of 2100 capacitors, with each capacitor rated at 43 μf . Although their maximum potential voltage is 12 kV the capacitors are only charged to 6 kV in view of their unknown life history. At 6 kV the total stored energy is therefore 1.6 MJ. The capacitors are distributed equally between three aluminum racks. When in parallel the impedance of each transmission line is 27 mOhms, yielding an inductance per section of 2.2 μH . The two-way transit time in the line is then 1.63 ms and the total current is 333 kA.

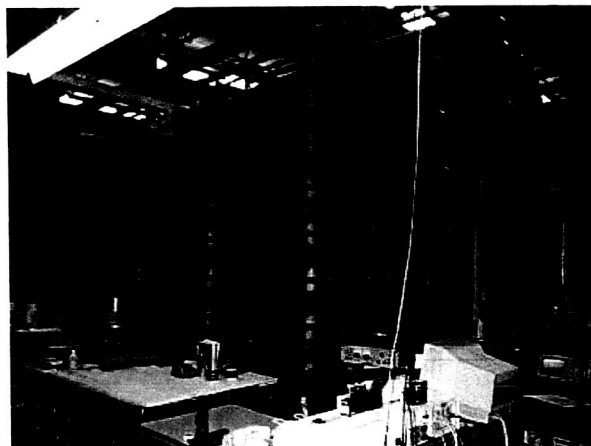


Figure 2-1. The Godzilla pulse forming network.

Plasma Source: To produce the plasma flow speeds necessary for emulating the fusion propulsion system, an existing inverse-pinch arrangement has been modified as shown in Figure 2-2². The present design has been guided by previous numerical simulations that aimed in ensuring that the discharge is confined at the minimum-area opening in order to minimize excessive heat transfer to the surrounding insulators, and to maximize the plasma exhaust speed.³ The accelerator consists of a 2.54 cm accelerating gap defined by inner and outer electrode radii of 22.9 cm and 25.4 cm, respectively. The distance between the outer electrode and the 20-cm vertical insulator is 11.2 cm.

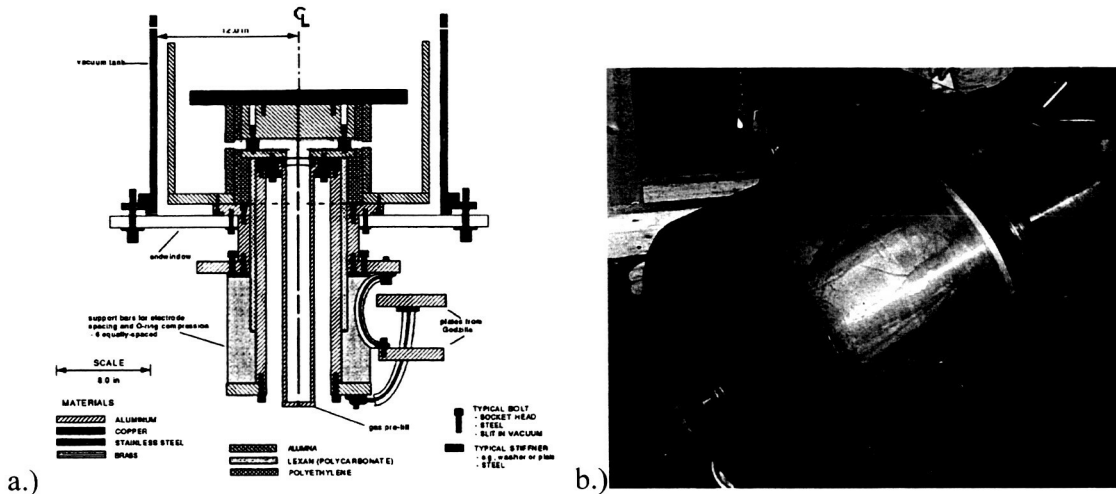


Figure 2-2. MPD plasma source for generating high velocity helium plasma. a.) Design. b.) Source.

Vacuum Facility: The MPD plasma source is mounted on one end of a 5.0 m long stainless-steel vacuum chamber with a diameter of .6 m. The vacuum chamber is evacuated to pressures of 10^{-5} torr prior to discharge using a 8" diffusion pump. Prior to firing, the diffusion pump is isolated from the chamber. The gas is injected from a large external reservoir through a calibrated, choked orifice. Flow is initiated by breaking the diaphragm at the exit of the reservoir. The discharge is initiated by Paschen breakdown across the electrodes when the gas flow reaches the interelectrode region. The vacuum facility is shown in Figure 3, with the propellant injection plenum identified in the foreground. For low power operation, a Lexan endplate is used at the far end of the vacuum chamber to allow direct observation of the discharge. At higher powers, a 1/2" steel plate is installed for safety. The vacuum facility is shown in Figure 2-3.

Mass Injection System: In "low power" (1-10 MWe) MPD thruster experiments performed by other researchers^{4,5}, the mass injection system and power system are operated on two different time scales – the propellant mass flow is initiated first, followed by the closing of a switch to connect the pulse forming network to the thruster. However, at the high power levels considered in this research (hundreds of MWe), using separate mass injection and power switching systems to operate the source is infeasible. Instead, the source is the switch to discharge the pulse forming network to ground.

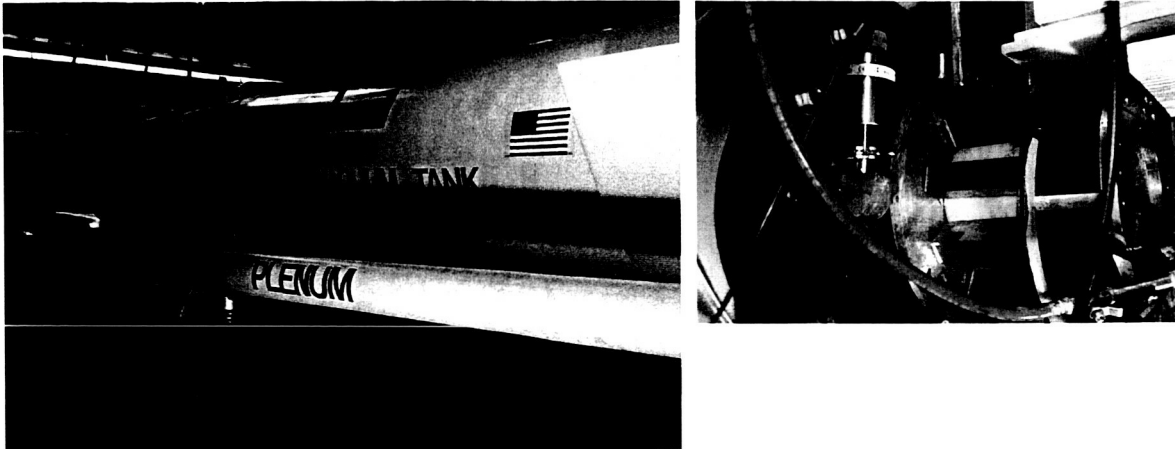


Figure 2-3. Plasma source vacuum facility: 5 m long, .6 m diameter, 10^{-5} torr before initiation of discharge.

Mass flow is regulated by choked flow of helium from a pre-filled plenum through the accelerator. By choking the gas flow, the mass flow rate is determined by the plenum pressure and the area of the choking point, according to isentropic, steady state, 1-D gas dynamics relationships:

$$\dot{m} = \frac{A_e P_0 M_e}{RT_0} \frac{\gamma}{\gamma-1} \sqrt{1 + \frac{\gamma-1}{2} M_e^2} \sqrt{\frac{\gamma RT_0}{1 + \frac{\gamma-1}{2} M_e^2}} \quad (2-1)$$

with $M_e = 1$ at the choking point. Choking is assumed to occur at the smallest area in the flow system. For some mass flow rates, the choking location and area could be controlled by installing throats of known area between the plenum and the plasma electrodes.

The mass injection system for the plasma source was revised from the system used in previous experiments to allow for improved operation in the anticipated magnetic nozzle experiments. The original configuration used a plenum/shock-tube injecting gas directly into the interelectrode region². This posed two difficulties for operation of the source at higher mass flow rate. First, the original plenum was sized to fit within the inner (cathode) support cylinder. This did not allow enough plenum volume for millisecond-long high flow rate pulses of helium. Second, the flow choked at a point inside the thruster channel, which required computational analysis to establish and verify the flow rates at different plenum pressures. The modified injection system consists of a larger (10 cm diameter, 2.4 m long) plenum, diaphragm followed by choked orifices of various sizes, and then the source. The full mass flow system is shown in Figure 2-3. Mass flow rates of 3-30 g/s had been identified computationally as desirable for the fusion simulation experiments; thin metallic foils were used as diaphragms, with the diaphragm thickness determining the burst pressure and therefore the mass flow rate.

Calibration of Mass Flow System: Prior to operation with the discharge, the mass flow system was calibrated using pressure probes located ~ 7 cm downstream of the orifice and (for cold flow) at the electrodes of the source. In order to measure flow rate, a Kistler piezoelectric pressure gauge was placed a few inches after the throat in the inlet flow path. Both static and total pressure measurements were taken for a variety of different diaphragms and chokes. A

lower mass flow rate was calculated using area ratios because it approached the lower limit of static pressures that could be measured by the Kistler gauge. A higher mass flow rate was also estimated by pressure ratios because it was near the limit of the plenum's maximum pressure. The primary mass flow calibrations were also later examined theoretically and numerically by Arizona State University. The results of this modeling are described in the computational section of the report.

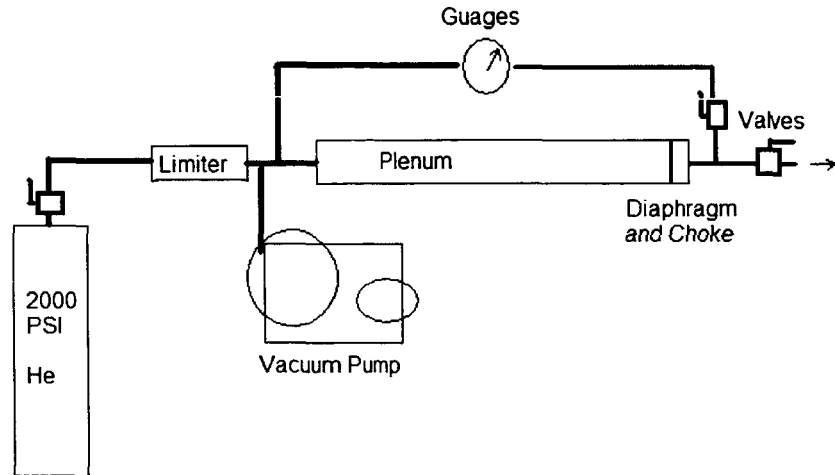


Figure 2-4. Schematic of plasma source mass injection system.

The operation of the source therefore proceeds as follows:

- 1) A diaphragm with the appropriate bursting pressure is installed in the mass flow system.
- 2) The vacuum chamber is evacuated to 10^{-5} torr, below the Paschen breakdown pressure for the 1-6 kV capability of the PFN. The plenum and mass flow system are also evacuated.
- 3) The PFN is charged to the desired voltage for the discharge.
- 4) The diffusion pump is isolated from the chamber using a pneumatically actuated gate valve to prevent damage to the pump from the high chamber pressure after a discharge.
- 5) Helium is fed into the plenum until the diaphragm bursting pressure is reached.
- 6) The gas breaks down across the electrodes and the discharge takes place.

The mass flow rates as calculated from pressure traces for some representative operating conditions are shown in Figure 2-5. The mass flow equilibrates after approximately 1 millisecond, which is midway through the discharge pulse. The quasi-steady characteristics presented in this work are therefore measured after the mass flow rate has reached the steady state value. Mass flows of .48, 6.45, and 27.8 g/s have been tested in this device.

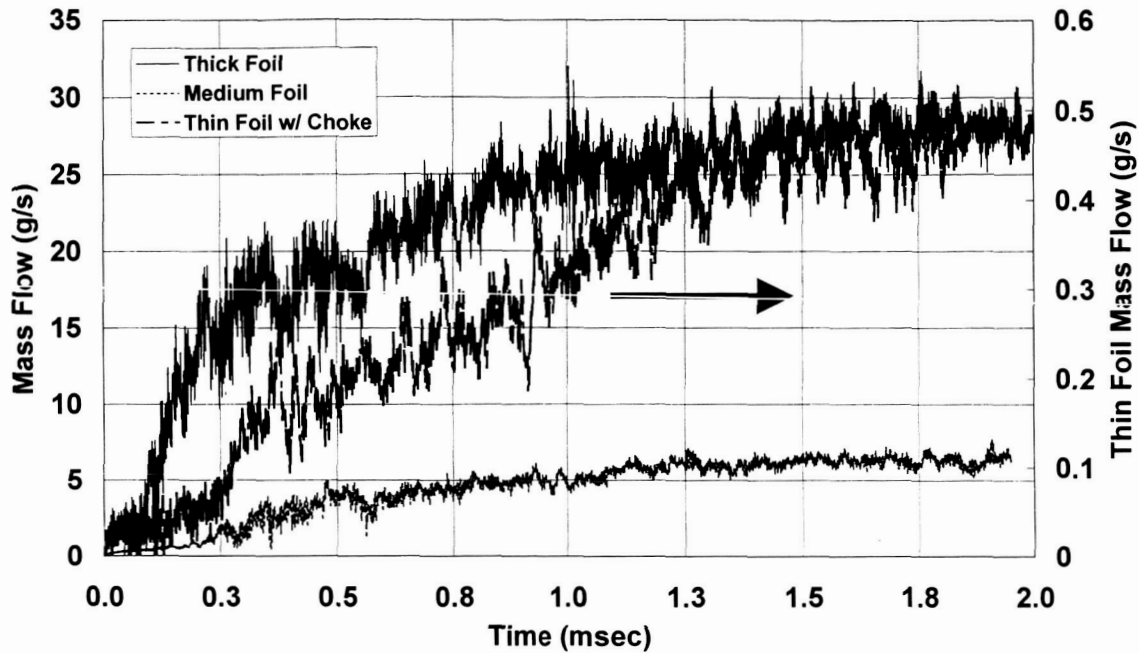


Figure 2-5. Sample mass flow temporal behavior from pressure measurements.

Diagnostics

The primary plasma source diagnostic is the measurement of the voltage drop across the source electrodes and measurement of the current through the source. Voltage was measured differentially using two Fluke 1000:1 high voltage probes attached to the anode and cathode of the thruster. The current was measured indirectly using a magnetic induction coil surrounding the current strap at the plasma source cathode. The induction coil measures the derivative of the current signal, which was then integrated computationally to obtain the current. These signals were taken by and stored on a Tektronix digital oscilloscope connected to the probes by shielded coaxial cabling.

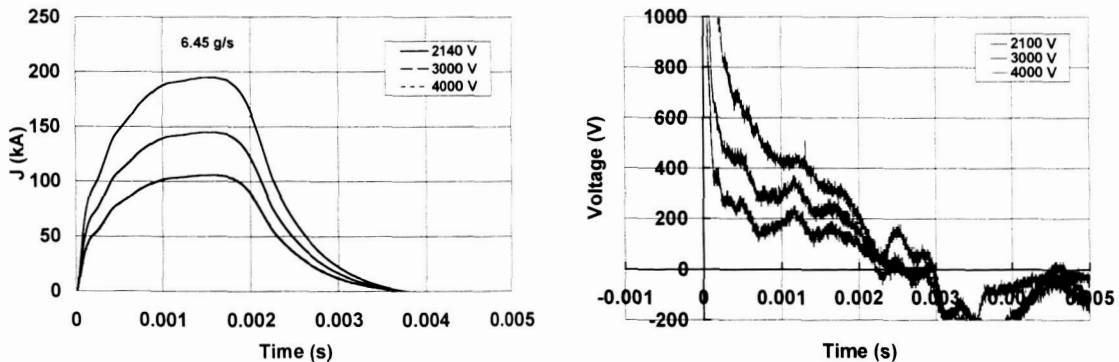


Figure 2-6. Sample discharge current and voltage traces for source operating at a mass flow rate of 6.45 g/s.

Some examination of the plasma plume was performed using triple Langmuir probes. These probes are able to measure plasma density and electron temperature simultaneously and in real

time. The triple probes, as their name suggests, consist of three collecting probe surfaces. Two of the probes are biased with respect to each other using a battery; the third probe is floating. The two probes and battery are also floating. By measuring the current flowing between the biased probes when they are immersed in the plasma, the voltage that the double probe system floats to, and the floating potential of the third probe, the plasma density and temperature can be calculated. Because of the high plasma temperatures, densities, and velocities inherent in this experiment, a limited data set of plume characteristics was obtained.

2.2. MPD Plasma Source Characterization

MPD Source Terminal Characteristics

The MPD source has been operated at helium mass flow rates from 0.4 g/s to 28 g/s. Helium was chosen to simulate the plasma “ash” resulting from a magnetically confined fusion reactor. Initial characterization of the discharge characteristics of the source over this range of mass flow rates has been achieved for source powers up to approximately 300 MWe. The steady state source voltage and power for currents up to 300 kA are shown in Figures 8 and 9, respectively.

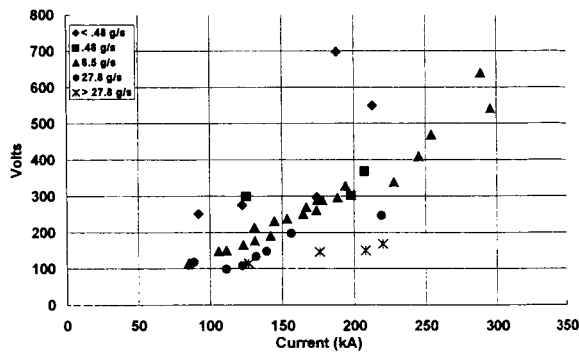


Figure 2-7. Voltage across MPD source electrodes for mass flow rates and currents spanning the operational regime.

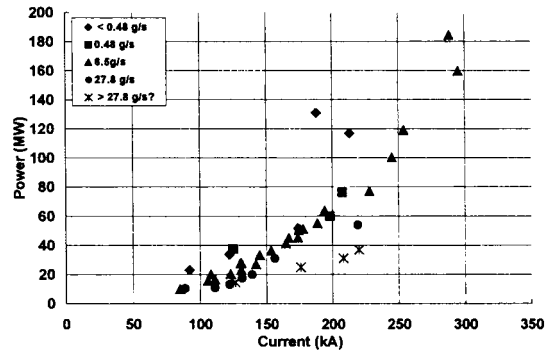


Figure 2-8. Power used by the MPD source for the same operational space as in Figure 7.

Although the source’s design goals are different than that of a MPD thruster, some of the physics hold true for both. An established theory of MPD thruster behavior is based on the Alfvén critical speed, $U_a = \sqrt{\frac{2eE_i}{M_i}}$ where E_i is the ionization energy of the propellant and M_i is the propellant atomic mass. For plasma speeds below, U_a , the plasma is predicted to be partially ionized; above U_a , the plasma is fully ionized. This bifurcation affects the thrust generation mechanism of the thruster, and through the thrust, the voltage and efficiency of the device⁶. Above U_a , the thrust is the well established electromagnetic thrust expression $T = bJ^2$, with the parameter “b” a function of the thruster geometry, $b = \mu_0 \frac{4}{\ln(\frac{R_a}{R_c}) + 1}$, where R_a is the anode radius, R_c is the cathode radius, and β is a constant accounting for current distribution over the cathode surface⁷. Below U_a , the thrust is linear with current. The current at which the propellant becomes fully ionized is called J_{fi} , and is defined as the current at which the fully ionized and partially ionized thrust expressions are equal: $J_{fi} = \sqrt{\frac{mU_a}{b}}$. The two thrust regimes are then

$$T = \begin{cases} \dot{m}U_a J/J_{fi} & u < U_a \\ bJ^2 & u > U_a \end{cases} \quad (2-2)$$

The contribution of the thrust power to the total discharge voltage is

$$\frac{T^2}{2\dot{m}J} = \begin{cases} bU_a J/2 & u < U_a \\ b^2 J^3 / (2\dot{m}) & u > U_a \end{cases} \quad (2-3)$$

so that the voltage characteristic should exhibit first a linear, then a cubic dependence on current. This behavior is shown in Figure 2–7. Only the tests at 6.45 g/s appear to have exceeded J_{fi} . The lower mass flow rates appear to have deviated from the assumptions of azimuthally symmetric discharges, resulting in a lower voltage at high currents. For mass flow rates greater than 6.45 g/s, the maximum operating currents were too low to exceed J_{fi} .

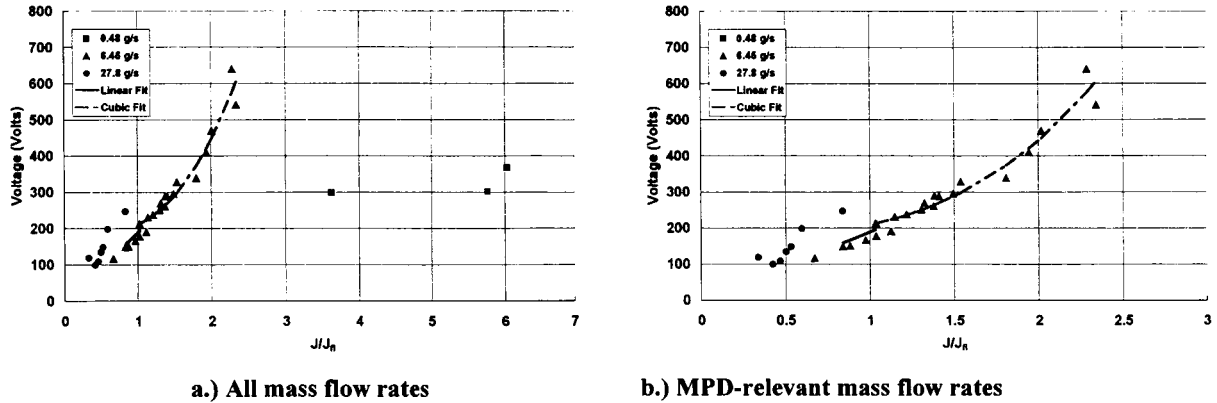


Figure 2–9. a.) Voltage with respect to normalized current using an estimated R_a/R_c of 1.185

The behavior of the source in light of the recent theoretically calculated mass flow rates is shown in Figure 2–9 for comparison. As an added uncertainty in modeling this behavior, the exact value of b , or more precisely, R_a/R_c , is unknown. However, this unknown can be addressed parametrically. Two effects result from the Alfvén critical speed hypothesis described earlier. The first is that there is a current value (J_{fi}) at which the voltage-current curve will transform from a linear to a cubic form. The second effect is that the coefficient of the cubic portion of the voltage-current has a coefficient of $b^2/2\dot{m}$. By iterating on a value of b and the resulting coefficient to J^3 for currents above J_{fi} , a self-consistent b value can be obtained. This analysis was performed on the data for 6.45 g/s, and obtained a b coefficient of $1.76 \times 10^{-8} \text{ N/A}^2$, corresponding to an effective R_a/R_c of 1.19. This is slightly larger than the geometric ratio of 1.10. The curve fits to these results are also shown in Figure 2–9. Theoretically, the linear slope below J_{fi} and the cubic slope above J_{fi} together should provide a unique solution to b ; however, the linear voltage region is affected by additional resistive voltage drops, so that the slope calculated there is not purely from the plasma acceleration. At higher currents, however, the cubic component of the voltage dominates and the slope there can be considered more strongly the result of plasma acceleration.

The analysis of the 6.45 g/s data was used to assess the 27.8 g/s data, which are shown in blue in Figure 2–9. The accuracy of the thrust-voltage scaling assumption is less clear with these data, as the operation is below J_{fi} for all points and other effects such as ohmic dissipation play a role in determining the voltage. By rearranging Equation 2-3 in terms of J/J_{fi} , the resulting slope is $\sqrt{mbU_A^3}/2$; the slope should increase with the square root of mass flow rate. The slopes of the two mass flow rate data are shown in Table 2–1, as well as their ratio and the square root of the ratio of the mass flow rates. As a qualitative indicator, the slope of the higher mass flow rate data is higher than the 6.45 g/s data, as shown in Table 2–1,.

	\dot{m} (g/s)		Ratio of slopes	$\sqrt{\dot{m}}$ ratio
	6.45	27.8		
Voltage-Current Slope ($J < J_{fi}$)	188.5	287.2	1.52	2.0

Table 2–1. Comparison of voltage-current behavior below J_{fi} for two mass flow rates.

Further, data at 0.45 g/s are shown at J/J_{fi} values greater than three. The low voltage observed at this mass flow rate implies that the discharge was not behaving as a MPD accelerator; instead, an asymmetric arc was probably formed. A spoke mode with higher plasma density in the spoke than for an azimuthally uniform discharge (the MPD mode) would not accelerate the plasma and the thrust energy contribution analyzed here would not appear in the voltage term.

Characterization of Plasma Exhaust

Plasma plume density was successfully measured by triple probe for one firing of the discharge at 6.45 g/s. This initial result is shown in Figure 2–10a. The plasma density reaches 10^{20} m^{-3} , which is near the value predicted using MACH2. Electron temperature was obtained over a range of mass flow rates and current levels. A sample measurement of electron temperature during a single pulse is shown in Figure 2–10b. The quasi-steady temperature measurements for several mass flow rates are shown in Figure 2–11, as functions of both current and J/J_{fi} . As with the voltage data, T_e is found to scale relatively straightforwardly with the normalized current, except for the lowest mass flow rates. At the low flow rates, the plasma is not an axisymmetric discharge and the generation and heating mechanisms involved are not consistent with MPD thruster operation. Under relevant operating conditions, T_e up to 15 eV were measured in the moving plasma at 6.45 g/s and 300 kA.

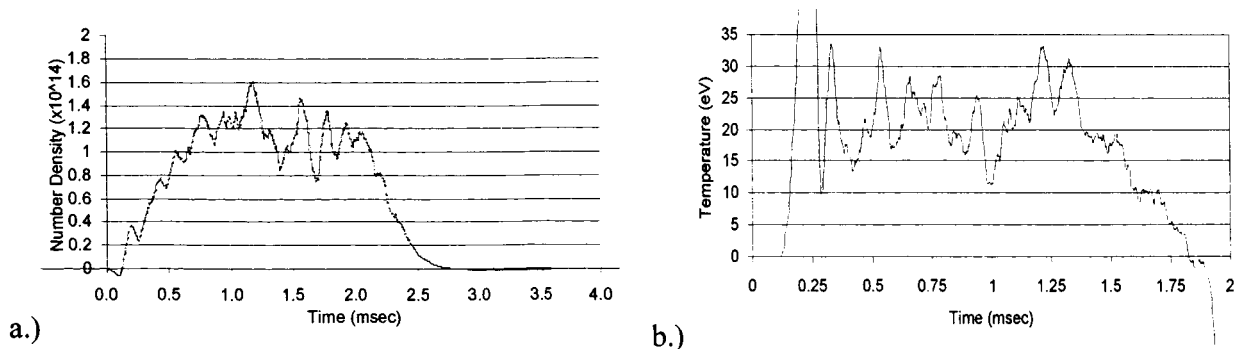


Figure 2–10. Sample density and T_e measurements using triple probes in plasma plume at 6.45 g/s.

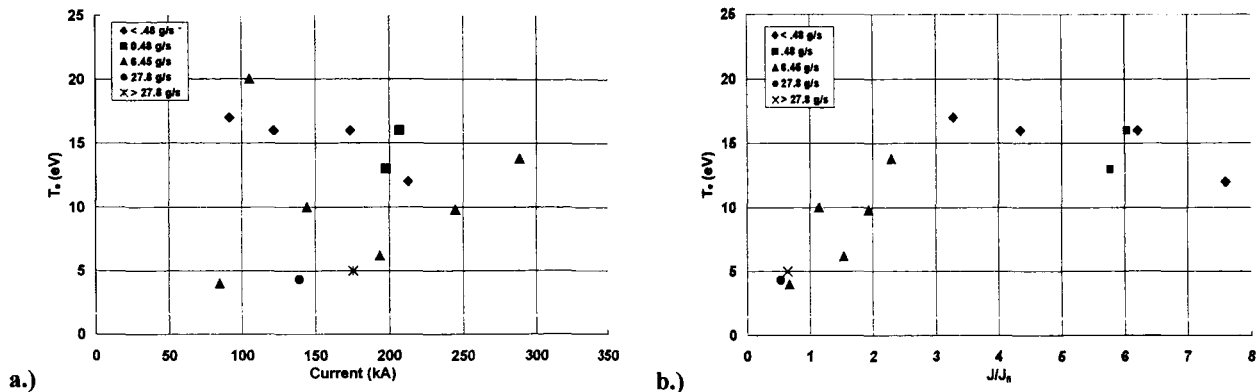


Figure 2-11. T_e scaling with operating current and mass flow rate (a), as well as scaling with normalized current (b).

3. Computational and Theoretical Modeling

3.1. MACH2 Code Description

The theoretical effort has utilized both analytical and numerical means to guide the design of the experiment. Numerical modeling of various sections has been performed using the unsteady, non-ideal, MHD code MACH2. The code solves the dynamic, single-fluid, MHD equations in two dimensions, rectangular or cylindrical-axisymmetric (while retaining all three spatial components of vector quantities). The computational mesh can be purely Eulerian, Lagrangian or Arbitrary. The code also includes phenomenological models for classical and anomalous transport that include the effects of anisotropy⁸. In order to gain specific insight into driving mechanisms and avoid the complexities associated with the coupling of multiple sections, each of the three main sections comprising the experiment has so far been simulated separately. Simulations of the MPD plasma source utilized a computational region that extended approximately 25 cm downstream of the interelectrode gap. Using an ideal current waveform that rose to a steady-state value of 300 kA in 30 μ s, iteration on initial conditions, geometry, mass flow rate and inlet flow profiles provided a final configuration (already described in the previous section), and operating conditions that achieved the desired output from the source.

3.2. Mass Flow System Model and Calibration

The nature of the mass flow system for the MPD source is necessarily complex due to the convoluted path the propellant must follow to reach the interelectrode gap. The varying channel areas and turns between the propellant plenum and the source introduce uncertainties in the flow speeds; particularly as to where the choking point of the flow to sonic conditions occurs. This path can be seen in Figure 3-1. The components and the processes occurring in them are described in more detail in the following discussion.

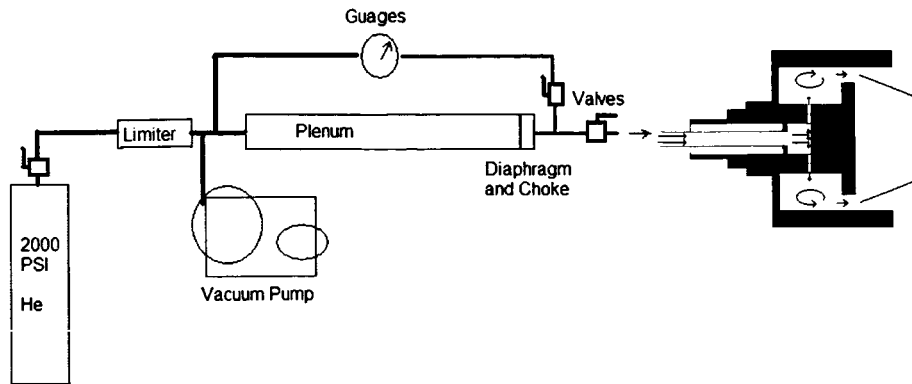


Figure 3–1. Schematic of propellant flow system and source, indicating the flow path simulated by computation.

Theoretical Analysis of the Helium Delivery System

The helium delivery consists of a 3.05-m plenum that is 10 cm in diameter. This plenum is fitted with one of three burst diaphragms whose thickness dictates the burst pressure. The three diaphragms are thin, medium, and thick foils to produce low, moderate, and high mass flow rates, respectively. Downstream of the diaphragm the flow is exhausted to a cylindrical channel of 0.97 cm-radius, that can accommodate various size constricting throats. Mass delivery to the discharge chamber is controlled by a main ball valve downstream of the diaphragm. The upstream (supply-side) and downstream (diaphragm-side) sides of the plenum are linked by a hose running from the helium supply tank up to the diaphragm-side of the plenum. Just downstream of the diaphragm but upstream of the main valve there is a separator ball valve that can be used to separate the two sides. In order to operate the helium delivery system, a small roughing pump lowers the backpressure to very low levels with the separator valve open so as to pump on both sides of the diaphragm equally. Once this is completed the separator valve is closed, the main valve is opened, and a 13.8-MPa-helium supply tank fills the plenum until the diaphragm bursts and helium flows into the discharge chamber. Stagnation pressure is measured by the pressure gauge just upstream of the main valve while exhaust static pressure is obtained well downstream of the main valve. Figure 3–1 shows a schematic of the helium delivery system with the significant components labeled, and Figure 3–2 depicts the total and static pressure traces obtained when the system operated with the thick diaphragm.

Due to the noise level in the experimental stagnation and static pressure data, the idealized analysis proceeds by averaging each data set to obtain a steady-state value. Specifically, a set of data points representative of the steady-state portion of the pressure traces were averaged over time as follows:

$$P_{average} = \frac{\Delta P dt}{\Delta t} = \frac{\Delta t \Delta P_i}{t} \quad (3-1)$$

where Δt is the constant data-sampling time increment, P_i is a measured pressure value, and t is the total sampling time.

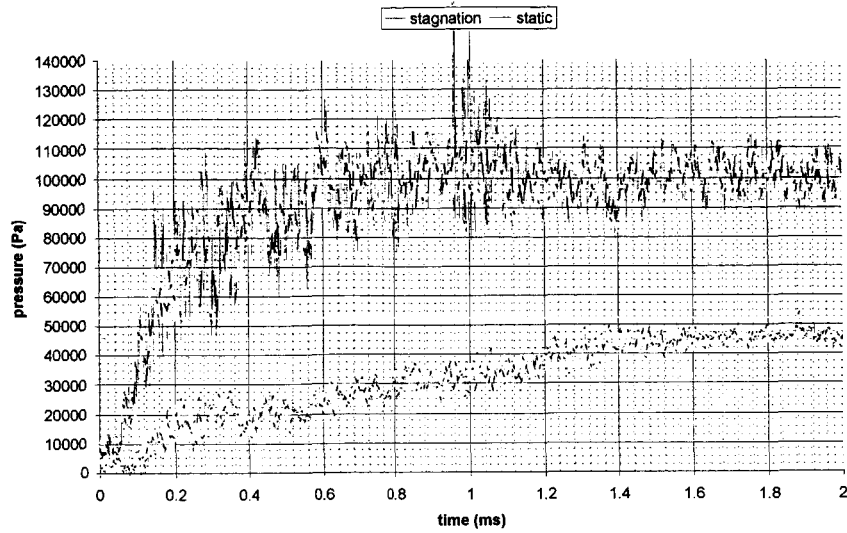


Figure 3-2. Experimental stagnation and static pressure traces for the thick foil diaphragm.

Once the average values for the stagnation, P_0 and static, P_e pressures for each diaphragm were computed, the idealized steady-state exit mach number, M_e could be obtained assuming isentropic, steady, quasi-1D flow from the ratio of stagnation to static pressures as shown below:

$$\frac{P_0}{P_e} = \frac{\gamma}{\gamma} \left(1 + \frac{\gamma - 1}{2} M_e^2 \right)^{\frac{\gamma}{\gamma - 1}} \quad (3-2)$$

$$M_e = \sqrt{\frac{2}{\gamma - 1} \left[\left(\frac{P_0}{P_e} \right)^{\frac{\gamma - 1}{\gamma}} - 1 \right]} \quad (3-3)$$

where $\beta = 5/3$ is the ratio of specific heats for helium. Based on the pressure averages calculated from Equation 3-1, Equation 3-3 indicates that the flow in all three cases is sonic or less at the exit. The thin, medium, and thick foil mach numbers were computed to be 0.745, 1.032, and 1.072, respectively. These results imply that the experiment was conducted using a constant-area channel downstream of the diaphragm for the two latter cases. In the cases of the medium and thick foils the flow was choked at the exit while for the thin foil case, the flow was subsonic throughout which does not allow determination of whether a variable-area duct was employed.

To compute the idealized mass-flow rates for each of the three diaphragm cases, the mass-conservation principle is invoked as follows:

$$\dot{m} = \rho u A = \rho_e u_e A_e \quad (3-4)$$

where β , u , and A are density, velocity, and channel area, respectively and the subscript e represents the exit conditions. Assuming ideal gas with constant ratio of specific heats and the definition of sound speed, equation 3.4 becomes

$$\dot{m} = \frac{P_e}{RT_e} M_e \sqrt{\gamma RT_e} A_e \quad (3-5)$$

For isentropic, steady, quasi-1D flow the temperature at the exit, T_e is a function of the stagnation temperature, T_0 and the exit mach number,

$$\frac{T_0}{T_e} = 1 + \frac{\gamma - 1}{2} M_e^2 \quad (3-6)$$

Substitution of the above exit temperature relation into equation 3-5, results in a general expression for calculating the mass flow rate through a nozzle within the isentropic, steady, quasi-1D assumption in terms of the relevant quantities A_e , M_e , P_0 , and T_0 :

$$\dot{m} = \frac{A_e P_0 M_e}{RT_0} \sqrt{\frac{\gamma}{1 + \frac{\gamma - 1}{2} M_e^2}} \sqrt{\frac{\gamma RT_0}{1 + \frac{\gamma - 1}{2} M_e^2}} \quad (3-7)$$

Using the experimental stagnation pressure averages along with the obvious presumption of sonic flow at the exit for the thick and medium foils the idealized exit pressure values can be computed,

$$P_e = \frac{P_0}{\sqrt{1 + \frac{\gamma - 1}{2} M_e^2}} \quad (3-8)$$

along with the desired mass-flow rate values. They are summarized in the table below with the thin-foil, subsonic-flow case utilizing the experimentally averaged exit pressure value.

	P_0 (Pa)	P_e (Pa)	M_e	\dot{m} (g/s)
Thin Foil	1820.3	1190.4	0.745	0.477
Medium Foil	23207.5	11305.3	1	6.450
Thick Foil	99865.6	48648.5	1	27.753

Table 3-1. Idealized model quantities for the thin, medium, and thick foil cases.

Confirmation of these values follows by employing the unsteady, 2-D axisymmetric, magnetohydrodynamics code, MACH2. Experimental discussions to date have implied that during operation with the thin-foil a so-called “small-choke” was utilized which implies that it is impossible to model the geometry unless the throat dimension is known. In addition, such low mass-flow rate values would not be used in operating the electromagnetic system at the maximum energy of 1.6MJ, thus no modeling will be performed for this case.

MACH2 Modeling of the Helium Delivery System

In the actual helium cold flow tests, both static and stagnation pressures were measured as a function of time for each of the three diaphragms so that mass flow rate could be computed after

each test, therefore pressure and mass flow rate are the quantities of interest in the numerical simulation. In MACH2 there is a utility that allows both pressure and mass flow rate to be computed at any axial location.

The previously-calculated stagnation pressure averages for each of the three diaphragms were used to determine the initial plenum pressures to be used for the MACH2 simulations. MACH2 incorporates boundary conditions in terms of density and temperature instead of an explicit pressure input to simulate flow and since density is not explicitly measured experimentally, the initial density of the flow simulating plenum conditions was calculated based on the average stagnation pressure using the ideal gas law:

$$\rho_0 = \frac{P_0}{RT_0} \quad (3-9)$$

where $R = 2077.23 \text{ J/kg-K}$ is the specific gas constant for helium and $T_0 = 288 \text{ K}$ is the plenum stagnation temperature. The initial stagnation densities were calculated to be 0.003 kg/m^3 , 0.039 kg/m^3 , and 0.167 kg/m^3 for the thin, medium and thick foil cases, respectively.

Based on these density values and the previously calculated mass flow rates from Table 3.1, an estimate for the pulse time was made for each of the cases as follows:

$$t_{pulse} = \frac{\rho_{0_{He}} V_{plenum}}{\dot{m}} \quad (3-10)$$

where $\rho_{0_{He}}$ is the stagnation density of the helium, V_{plenum} is the plenum volume, and \dot{m} is the helium mass flow rate. This analysis yielded pulse times of approximately 0.15 s for the three cases. These pulse times are more than two orders of magnitude greater than the current discharge pulse time of about 1.6 ms and the associated transient duration indicated by the experimental pressure traces of about 2 ms. This implies that the magnetoplasmadynamic source will operate at the steady-state, predetermined mass flow-rate value for the duration of the discharge, thus eliminating the risk of damaging any of the source components due to excess temperature. (Unless of course breakdown occurs during the transient portion of the mass pulse which could be detrimental if the discharge and pressure distribution are azimuthally uniform. It is however, more likely that if insufficient gas mass is provided with pressure variations, the discharge will be localized, i.e. arcing will occur.) Furthermore, this implies that the plenum is indeed large enough to be considered of infinite dimensions, (along with expansion wave transit times of the order of 3 ms), which results in the ability to implement a constant-pressure boundary condition in the simulation. This condition was used in lieu of the actual plenum geometry in the interest of computational efficiency.

The MACH2 simulation domain was composed of the constant-area axisymmetric channel, which was exhausted into a diverging section and then to a larger constant-area channel to emulate the vacuum chamber. This allows comparison to both the idealized mass-flow rate values and the experimentally obtained exit pressure values as the latter needs not be an input quantity. A representation of the computational domain is shown in Figure 3-3 identifying the block structure used to construct the geometry. The simulation domain contained three blocks. The fluid was modeled as ideal gas with insulating thermal and free-slip velocity boundary conditions.

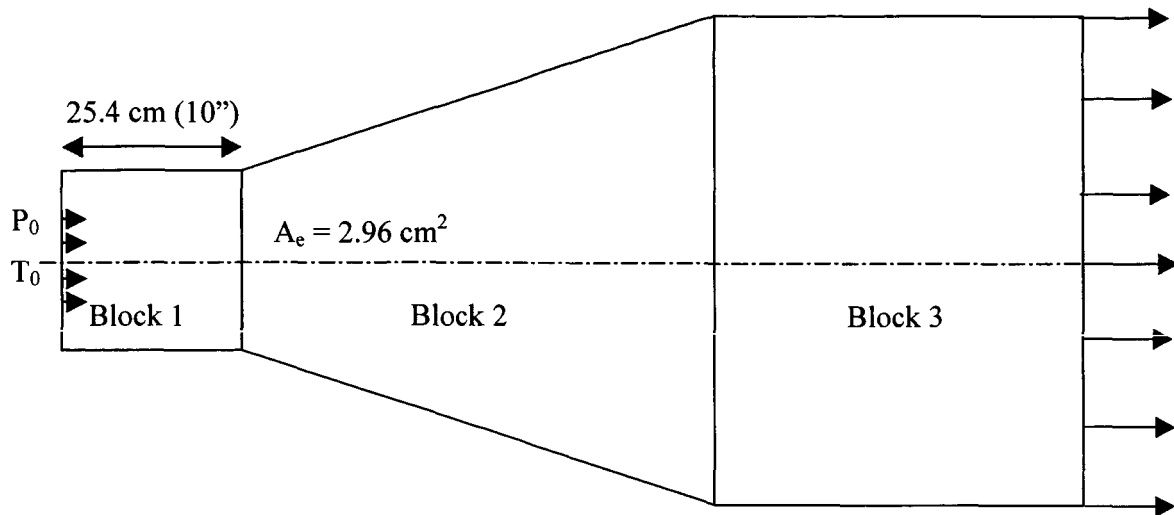


Figure 3-3. Computational domain for modeling mass flow system.

In order to establish the length of the constant-area channel that corresponds to the same rise times in the experimental data, an asymptotic relationship was assumed for the progression of the exit pressure to the steady-state value. Assuming that

$$\frac{P_e(t)}{(P_e)_{ss}} = e^{-\frac{\tau}{t}} \quad (3-11)$$

where $P_e(t)$ is the instantaneous exit pressure and $(P_e)_{ss}$ is the steady-state pressure value computed above in Table 3-1, and since the characteristic transit time is

$$\tau = \frac{l}{\sqrt{\gamma RT_0}} \quad (3-12)$$

the length of the channel can be approximated by

$$l = \gamma \sqrt{\gamma RT_0} t_{rise} \ln \frac{P_e(t)}{(P_e)_{ss}} \quad (3-13)$$

where $t_{rise} \sim 2$ ms is the experimental rise time of the pulse. Finally, by choosing $P_e(t)$ equal to some percentage of the steady-state pressure value, the length can be estimated. By using a 90% approximation of the steady-state exit pressure value, a length of approximately 25.4 (10³) cm was computed.

The time-dependent exit pressure and mass flow rate from the three cases were plotted from the beginning of the pulses to 2 ms corresponding to the experimental trace times. This gives a complete view of the transient and quasi-steady regimes of operation, clearly showing the quasi-steady pressure and mass flow rate values as can be seen in Figures 3-4 and 3-5.

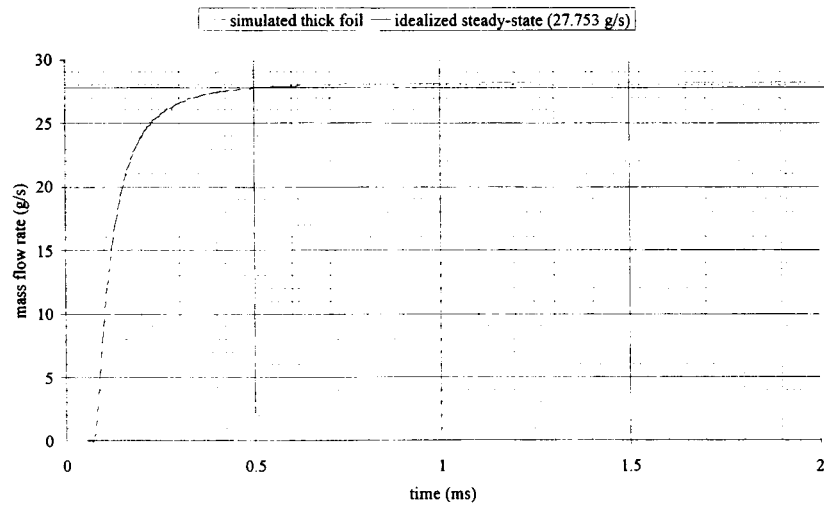
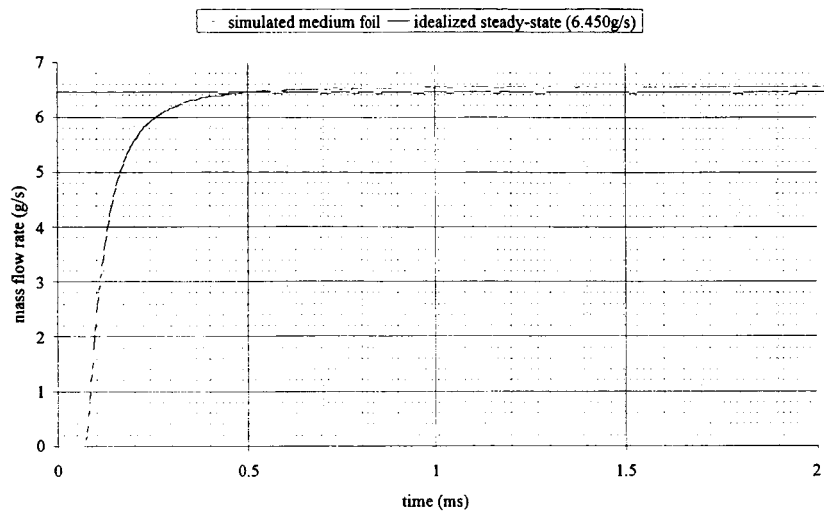


**Figure 3–4. Plots of simulated mass flow rate versus time for the medium and thick foil cases.
 Top: medium foil – 6.554 g/s. Bottom: thick foil – 28.196 g/s.**

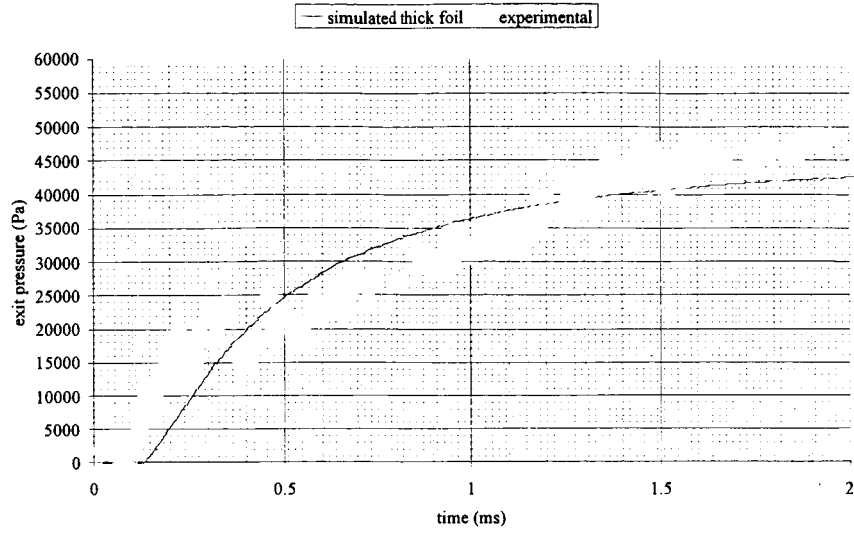


Figure 3-5. Plots of simulated and experimental exit pressure versus time for the thick foil case.

The two-dimensional, unsteady MACH2 modeling of the mass-feed system provides the necessary validation for use of the isentropic, steady-state, quasi-1D approximation for further design and refinement. It is thus useful to compute the necessary stagnation pressure, P_0 and thus the proper choice for the diaphragm foil, for the originally designed mass-flow rate value of 12g/s. Substitution of Equations 3-8 and 3-6 into equation 3-5 and some algebra provides P_0 as a function of \dot{m} , T_0 , M_e , and A_e ,

$$P_0 = \frac{\dot{m} R T_0 \frac{\gamma}{\gamma-1} \left[1 + \frac{\gamma-1}{2} M_e^2 \right]^{\frac{\gamma}{\gamma-1}}}{A_e \sqrt{\frac{\gamma R T_0}{1 + \frac{\gamma-1}{2} M_e^2}}} \quad (3-14)$$

By setting $M_e = 1$, equation 3.11 can be used as a design equation based on the current configuration of the experimental setup, wherein a constant-area channel is used. Thus, the required $P_0 = 43,179.9$ Pa was computed for the design point mass flow rate of 12 g/s.

3.3. Magnetic Nozzle Performance and Design Calculations

In order to gain specific insight into driving mechanisms and avoid the complexities associated with the coupling of multiple sections, each of the three main sections comprising the experiment has so far been simulated separately. Simulations of the MPD plasma source utilized a computational region that extended approximately 10 in downstream of the interelectrode gap Using an ideal current waveform that rose to a steady-state value of 300 kA in 30 μ s, iteration on initial conditions, geometry, mass flow rate and inlet flow profiles provided a final configuration (already described in the previous section), and operating conditions that achieved the desired output from the source. Specifically, it was shown that helium gas at a chamber density of 3.5e-5 kg/m³, provided at a rate of 13 g/sec would lead to confinement of the arc discharge along the

accelerating. The model suggests that this configuration provides thrust values in excess of 1.3 kN and exhaust speeds in the order of 100 km/sec. The configuration also yielded temperatures in the MPD chamber that should be tolerated by the vertical insulator (<1700 K).³

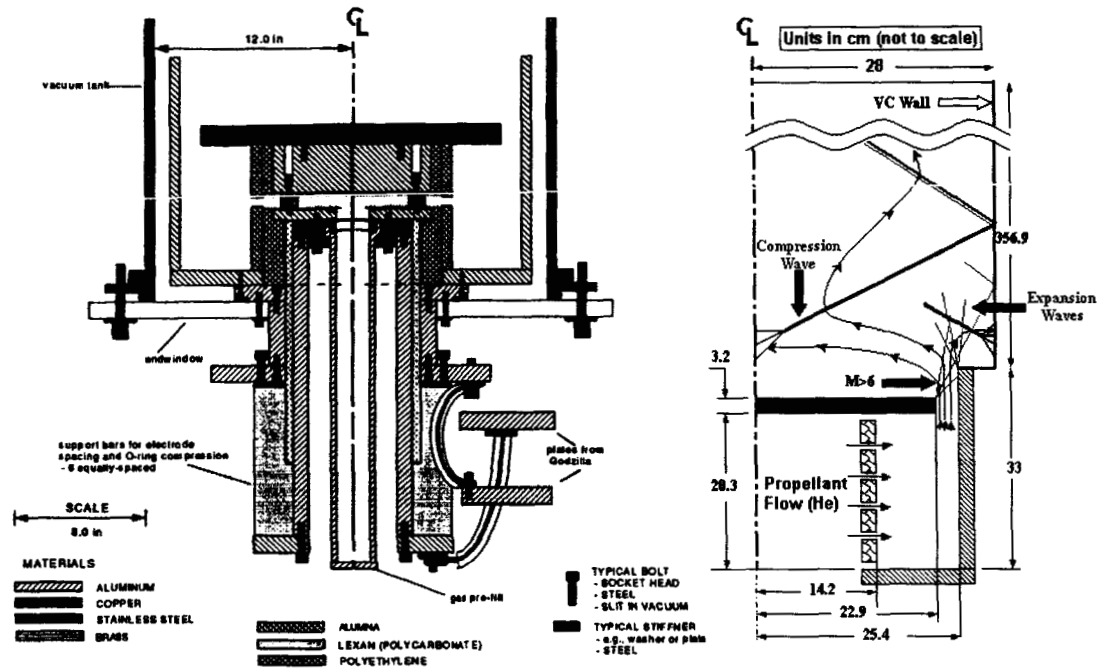


Figure 3-6. Schematic of the MPD plasma source showing the computational region used for numerical simulations.

MACH2 was utilized to simulate plasma flow using an extended computational region downstream of the MPD plasma source. The simulations gave a quantitative picture of the wave patterns expected upon interaction of the hypersonic plasma from the source with itself and the surrounding boundaries.⁹ The downstream compressions waves lead not only to loss of total pressure but also to redirections of the plasma flow downstream of the source orifice. The latter is especially critical in the design of the coil geometry.

Timing was also found to be an issue. Simulations without the magnet coil “on” suggested that the desired plasma flow conditions at the electrode gap were attained long after the current rise time, at approximately 100 microseconds (see Figure 3-7). Although placing the coil in series with the plasma source is favorable because it would allow the magnetic and velocity fields to build-up “in-sink” downstream of the source orifice, it does not alleviate the possibility of choking the flow at the desired throat point if the magnetic pressure there is designed based on the steady-state flow conditions. Simulations with a magnetic field that was applied at $t=0$ confirmed this notion and exposed its destructive consequences on the MPD source. In an effort to alleviate this time mismatch the opposite extreme was preliminary evaluated by applying the magnetic field after steady state had been reached as shown in Figure 3-8). In these simulations the coil was also placed closer to the gap. The results suggested that the plasma flow must be redirected further downstream (the peak pressure point along the centerline in the present MPD geometry is 30cm downstream of the inner electrode) because, in order to utilize most of the available flow energy in the present configuration, the coil must be placed so close to the gap

that the plasma beta there is much smaller than unity ($\beta=0.03$), which led to choked flow at the source orifice.

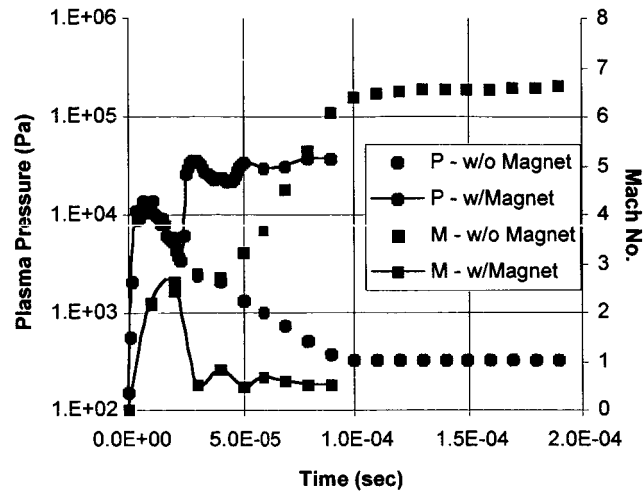


Figure 3-7. Evolution of plasma pressure and Mach number at the mid-gap location, w/ and w/o the coil (Coil tuned on at $t=0$ s).

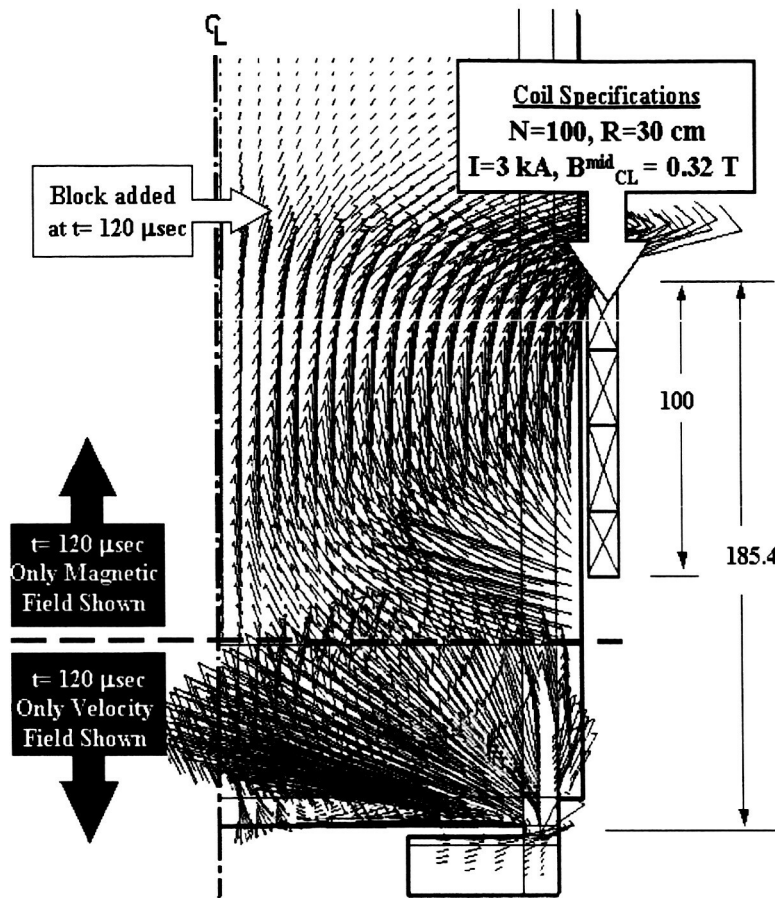


Figure 3-8. Steady-state velocity field and initial magnetic field applied by a 3-kA coil, shown at $t=120$ microseconds.

Numerical Simulations for the Design of the Secondary Magnet Coil

Exhaust Flow from the MPD Plasma Source Using Different Electrode Geometries (No Applied Magnetic Field)

Various geometrical electrode configurations have been simulated in an attempt to redirect the flow farther downstream of the MPD source orifice. Figure 3-9 shows a close up of the original electrode geometry (used in the previous effort), for comparison. This case will be referred to as case "G-0". Figure 3-10 shows an arrangement in which the inner electrode was made thicker by 3.25 in, reaching almost (but not quite) the height of the outer electrode. This set up was the first attempt to reduce the radial component of the $j \times B$ force ("pumping") downstream of the inner electrode which, by comparison to the gas dynamic force, drives the observed large divergence of the plasma flow exiting the interelectrode gap. Simulation cases using this geometry will be referred to as "G-1". Case "G-2" incorporates both a thicker electrode and a divergence angle of 75 deg and is shown in Figure 3-11. The last case, "G-3" shown in Figure 3-12, involves the same divergence angle but with a 14.25 in-thick electrode. An ultimate goal in the design of the MPD source was to operate with a discharge distribution Figure 3-13 top (the original case). The remaining cases shown in Figure 3-13 illustrate that

indeed this has been achieved for all three new geometries. The plasma temperatures along the ceramic insulator remain at sufficiently low values (~ 1000 K) for all cases.



Figure 3–9. Close-up view of computational region showing MPD source chamber and electrode arrangement in original configuration (Case “G-0”).



Figure 3–10. Close-up view of computational region showing MPD source chamber and electrode arrangement in case “G-1”.

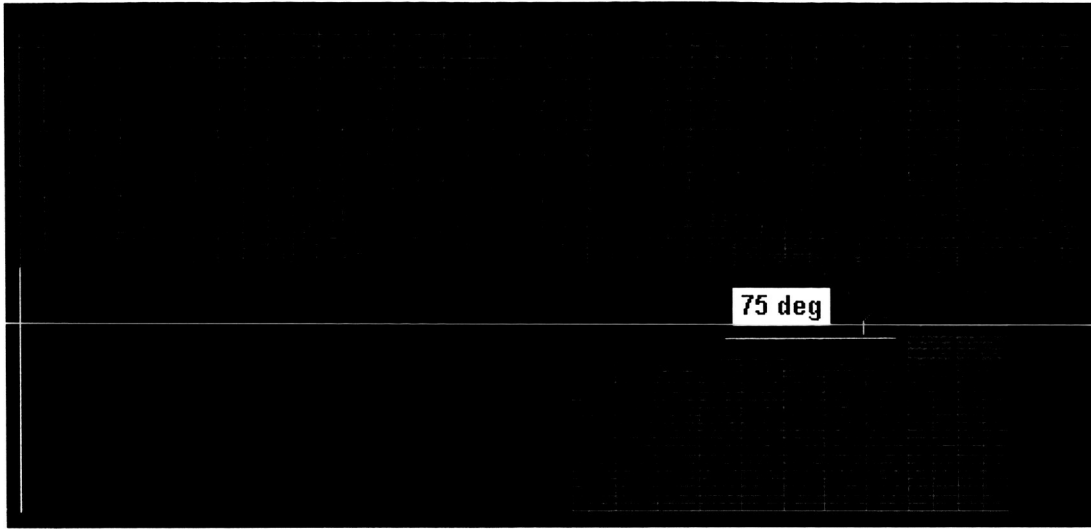


Figure 3-11. Close-up view of computational region showing MPD source chamber and electrode arrangement in case "G-2".

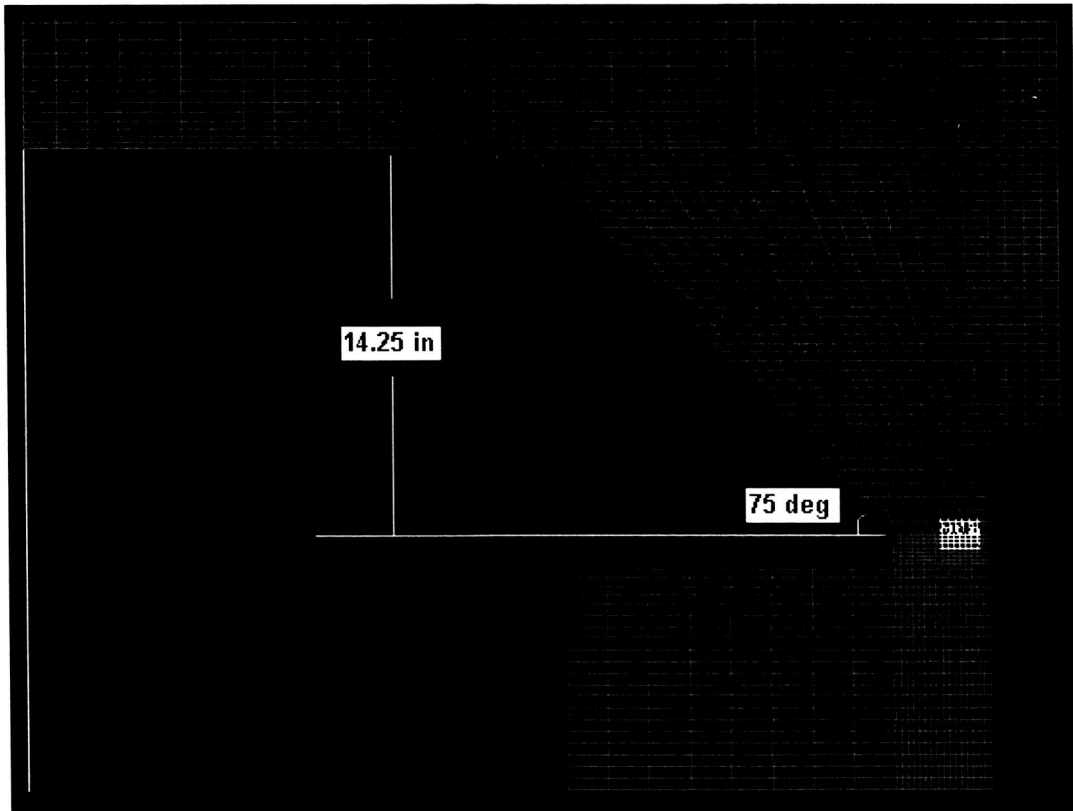


Figure 3-12. Close-up view of computational region showing MPD source chamber and electrode arrangement in case "G-3".

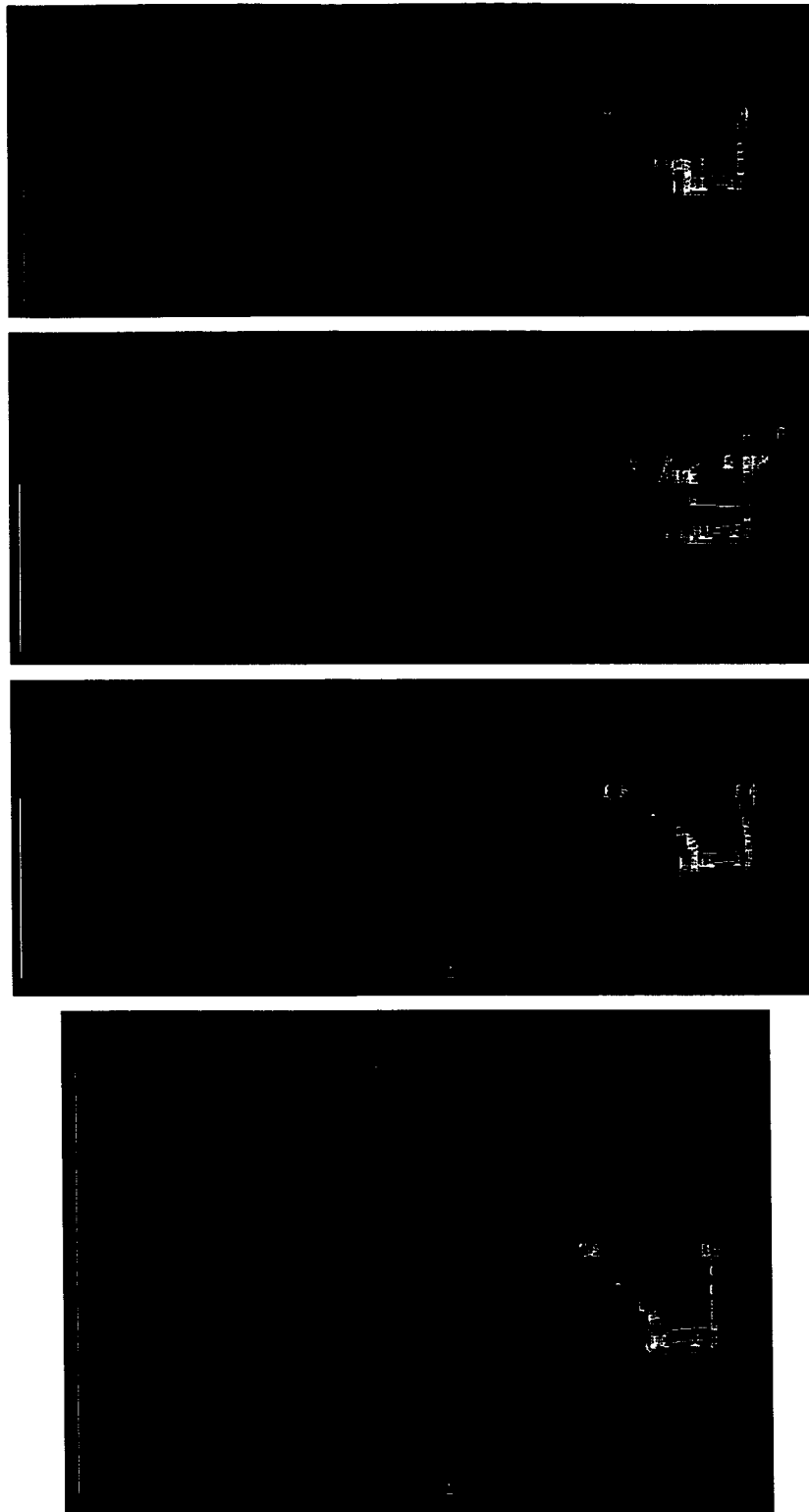
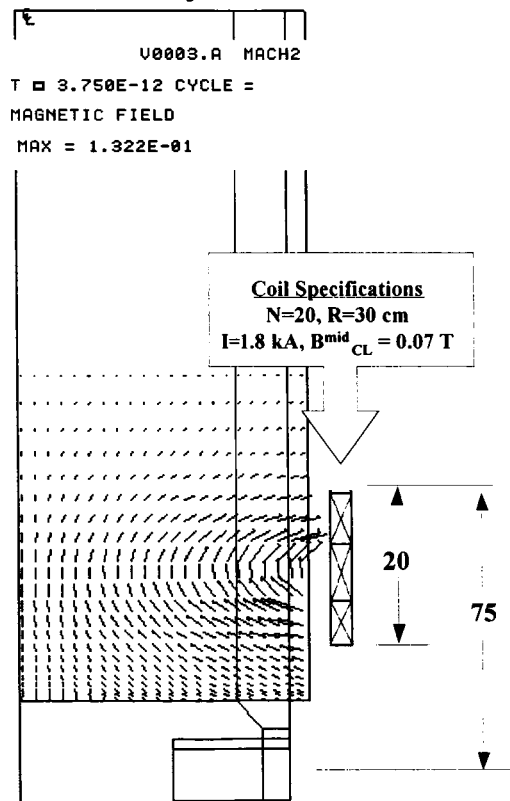


Figure 3-13. Computed current contour in steady state for the four different cases. From top to bottom the cases shown are G-0, G-1, G-2 and G-3, respectively.

Figure 3-14 and Figure 3-15 show plasma pressure contours and velocity vectors, respectively, for the various cases. By comparison to case G-0, G-1 results in minimal extension of the first compression point. The highest pressure point at the centerline is located only a few centimeters farther downstream of the location attained in the G-0 case. It was therefore decided that case G-1 will not be evaluated in any simulations with an applied magnetic field. Better progress was achieved in case G-2. Figure 3-16 shows the variation of plasma pressure close to the centerline as a function of axial distance (measured from the origin which is located approximately midway through the source chamber on the z-axis). It is shown that for case G-2, the peak compression point has been moved forward by about 20 cm compared to the G-0 case. As it will be shown later in this report, G-2 will be used in simulations with the coil turned on at $t=0$ sec. Case G-3 has produced even better results with the compression point located 50 cm farther downstream attained by the original configuration G-0.

Plasma Flow from the MPD Source with an Applied Magnetic Field

Magnet Coil Turned on at $t=0$ sec for Case G-2. An initial magnetic field distribution is



implemented as shown in

Figure 3-17 for case G-2. The coil magnetic field in this case is applied at $t=0$ sec, so it is assumed that the coil is powered by an independent power supply (i.e. it is not placed in series with MPD source). The coil specifications were determined based on the steady-state conditions achieved without the coil "on" (see previous section). Specifically, the peak initial magnetic field at the centerline was specified to be slightly less than the peak plasma pressure achieved in steady state. The location of the coil was such that the peak pressures (initial magnetic and steady-state plasma) were at approximately the same location. The length of the coil chosen so as to achieve an magnetic field at the MPD source orifice that is less than steady state plasma

pressure achieved at that location without the coil “on”. The (initial) magnetic and (steady state) plasma pressure profiles close to the centerline are shown in Figure 3–16.

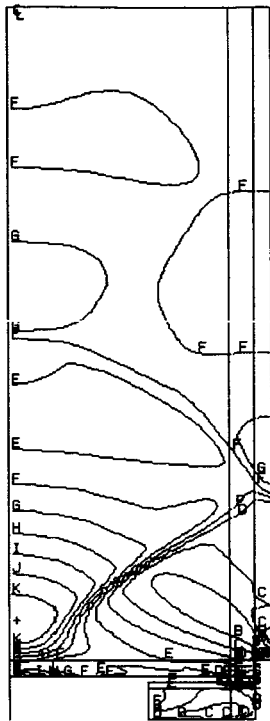
Figure 3–18 shows the evolution of plasma pressure midway through the electrode gap. By comparison to previous cases, e.g. see Figure 3–7, the flow at the gap is able to recover from the first compression wave occurring early in the simulation ($\sim 40 \mu\text{sec}$). However, a second stronger compression wave captured at approximately $110 \mu\text{sec}$ chokes the MPD flow without recovery. Unfavorable plasma conditions are computed by MACH2 along the ceramic insulator surface, similar to the case reported in ref 9. Plasma temperatures there are in excess of 10 eV. Both these simulations and the ones presented in the previous report point to a design that allows the flow to reach steady state before applying the magnetic field.

Magnet Coil Turned on After MPD Plasma Flow has Reached Steady State for Case G-3.

The results of the previous section motivated this next series of simulations that invoked the “Remap” option in MACH2. Figure 3–19 shows the simulation set up. The coil specifications were determined in the same way as in the simulations of section B.1. Figure 3–16 shows the initial magnetic pressure and steady-state plasma pressure close to the centerline as a function of distance from the origin. We note the decrease in peak plasma at the centerline in going from cases G-0 to G-2 and finally to G-3, confirming that plasma is delivered at the centerline along a larger area, i.e. more flow is delivered downstream compared to the original case, G-0.

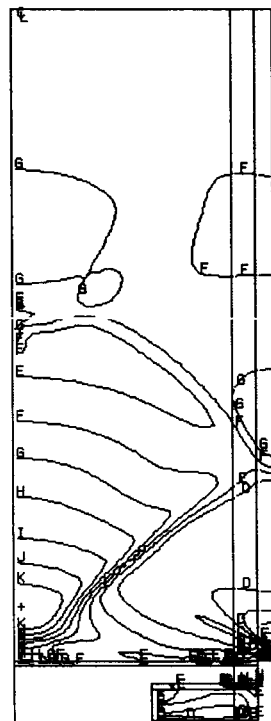
MPDWOCHGRDOFF
 T = 2.001E-04 CY
 TOTAL PRESSURE

-- 1.0043E+01
 A= 1.7778E+01
 B= 2.9148E+01
 C= 4.7789E+01
 D= 7.6353E+01
 E= 1.2847E+02
 F= 2.1063E+02
 G= 3.4534E+02
 H= 5.6628E+02
 I= 9.2832E+02
 J= 1.5220E+03
 K= 2.4955E+03
 += 4.0915E+03



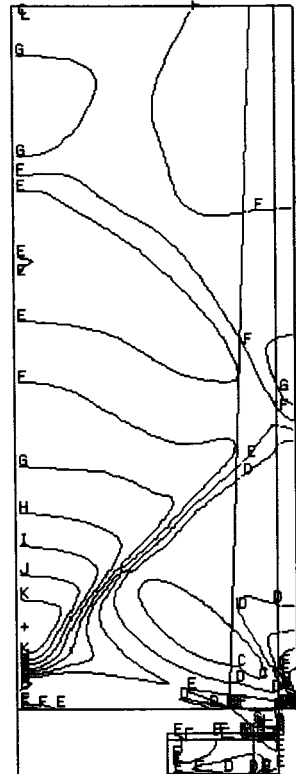
NOC U0003.A MACH2
 T = 2.000E-04 CYCLE □
 TOTAL PRESSURE

-- 9.7677E+00
 A= 1.5758E+01
 B= 2.5422E+01
 C= 4.1013E+01
 D= 6.6165E+01
 E= 1.0674E+02
 F= 1.7221E+02
 G= 2.7782E+02
 H= 4.4819E+02
 I= 7.2306E+02
 J= 1.1665E+03
 K= 1.8819E+03
 += 3.0360E+03



MPDWOCT
 T = 2.001E-04
 TOTAL PRESSURE

-- 7.6800E+00
 A= 1.2358E+01
 B= 1.9886E+01
 C= 3.2000E+01
 D= 5.1493E+01
 E= 8.2860E+01
 F= 1.3333E+02
 G= 2.1455E+02
 H= 3.4525E+02
 I= 5.5556E+02
 J= 8.9398E+02
 K= 1.4386E+03
 += 2.3148E+03



MPDWOCLT
 T = 2.000E-04
 TOTAL PRESSURE

-- 1.5784E+00
 A= 2.7028E+00
 B= 4.6288E+00
 C= 7.9247E+00
 D= 1.3578E+01
 E= 2.3236E+01
 F= 3.9787E+01
 G= 6.8128E+01
 H= 1.1666E+02
 I= 1.9976E+02
 J= 3.4205E+02
 K= 5.8578E+02
 += 1.0029E+03

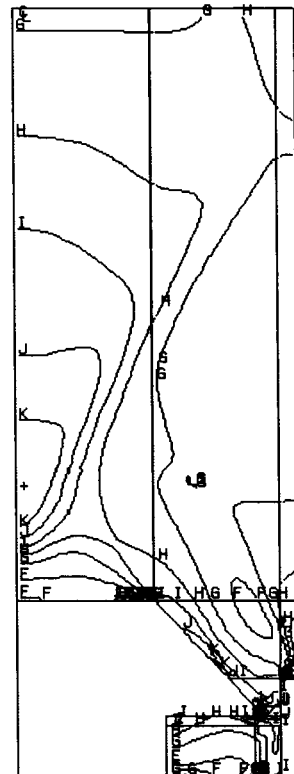


Figure 3-14. Computed pressure contours in steady state. Top left: case G-0. Top right: case G-1. Bottom left: case G-2. Bottom right: case G-3.

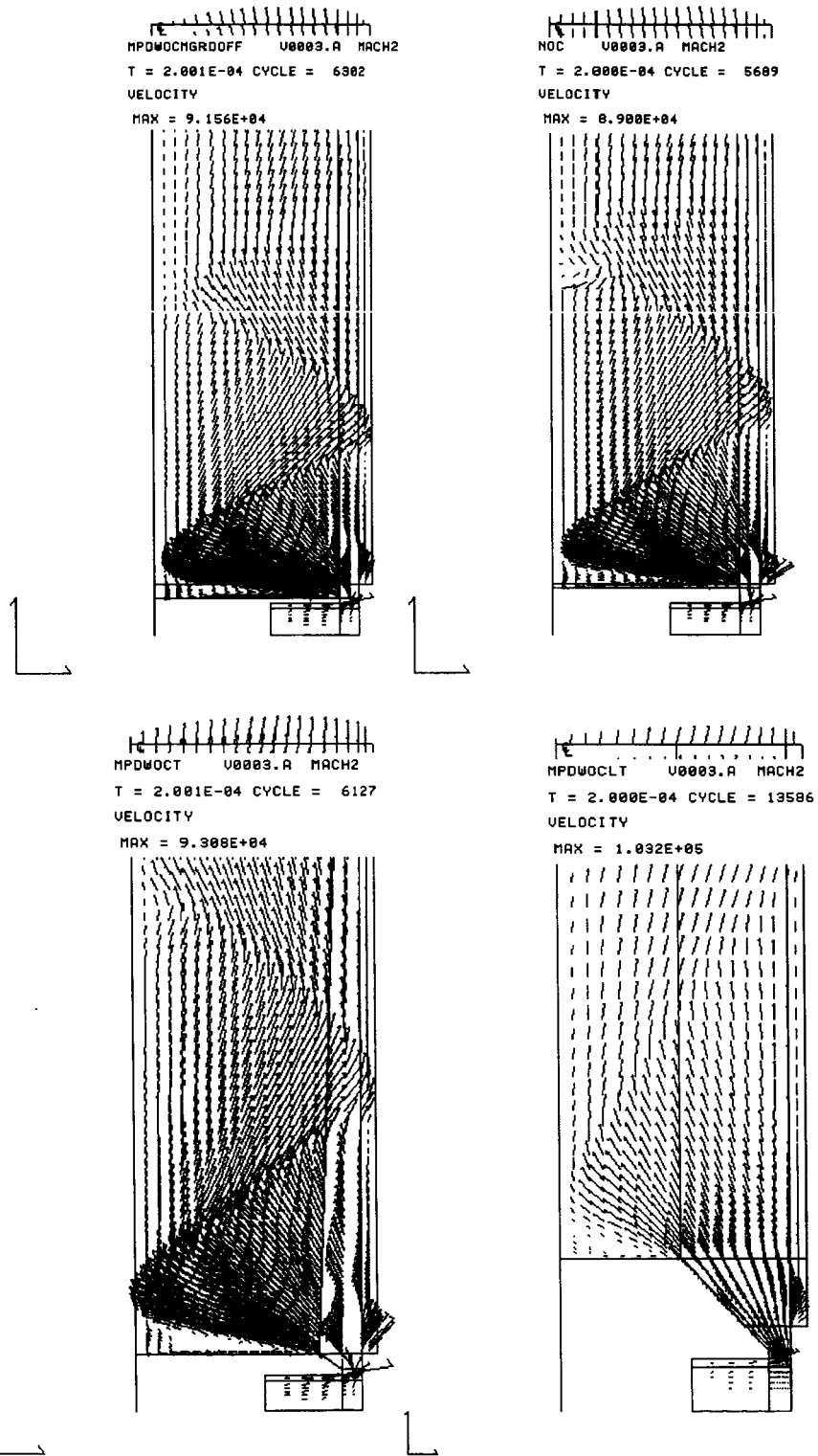


Figure 3-15. Computed velocity vectors in steady state. Top left: case G-0. Top right: case G-1. Bottom left: case G-2. Bottom right: case G-3

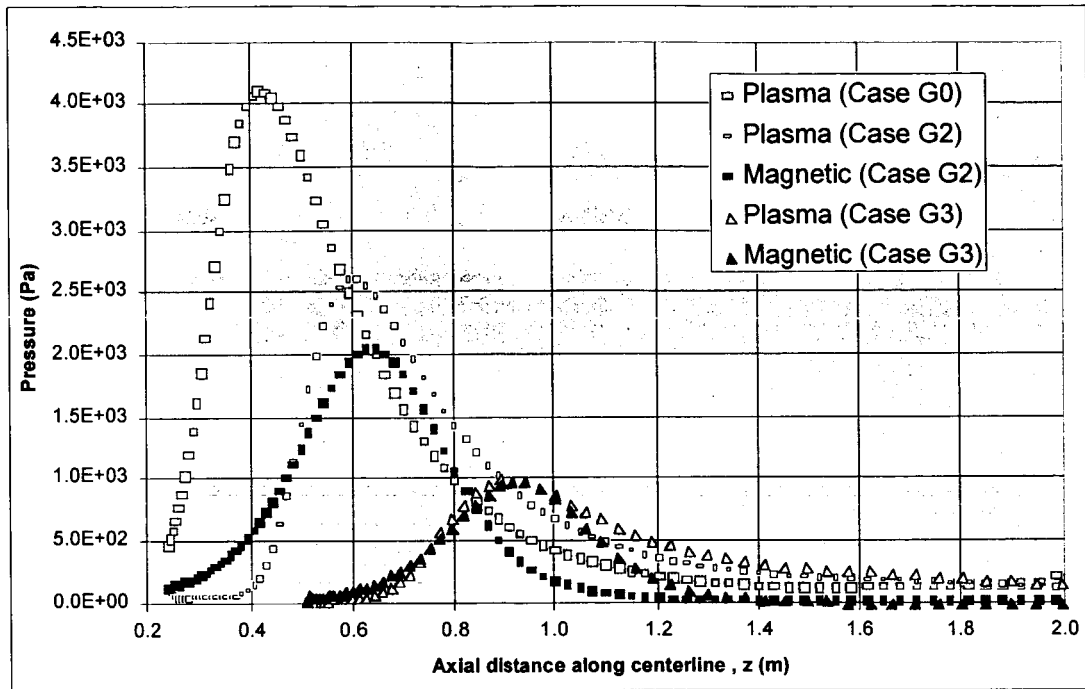


Figure 3-16. Pressure distribution along the centerline. Yellow points denote plasma pressure in steady state with no applied magnetic field. Blue points denote magnetic pressure due to the initial applied magnetic field.

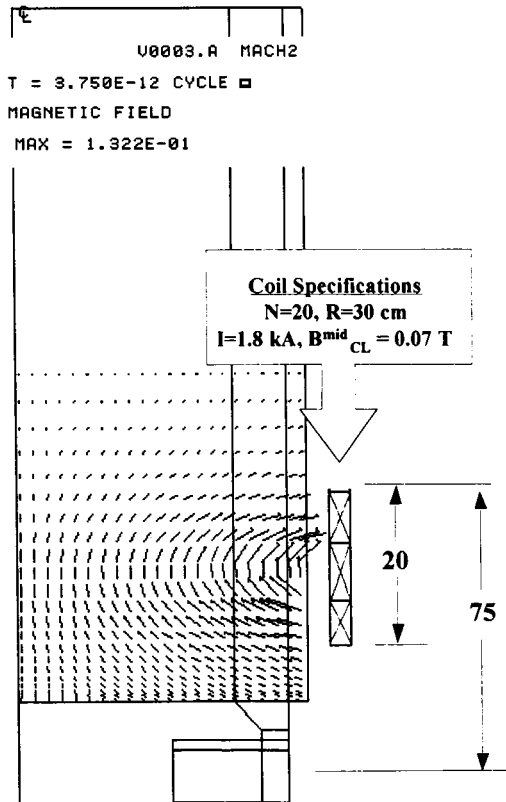


Figure 3-17. Coil specifications and initial magnetic field vectors for case G-2.

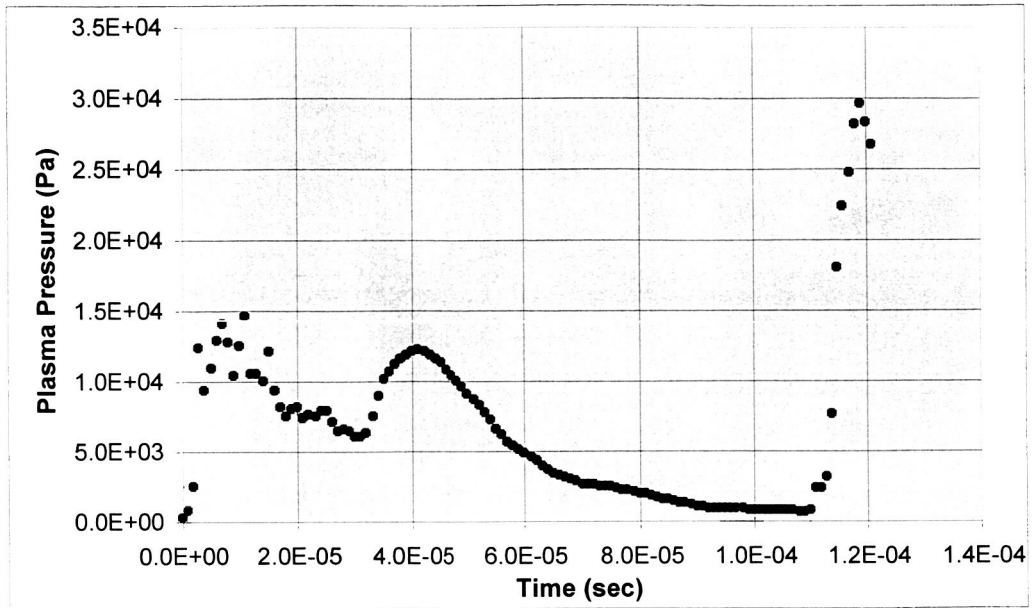


Figure 3-18. Pressure history at a point located midway through the electrode gap for case G-2.

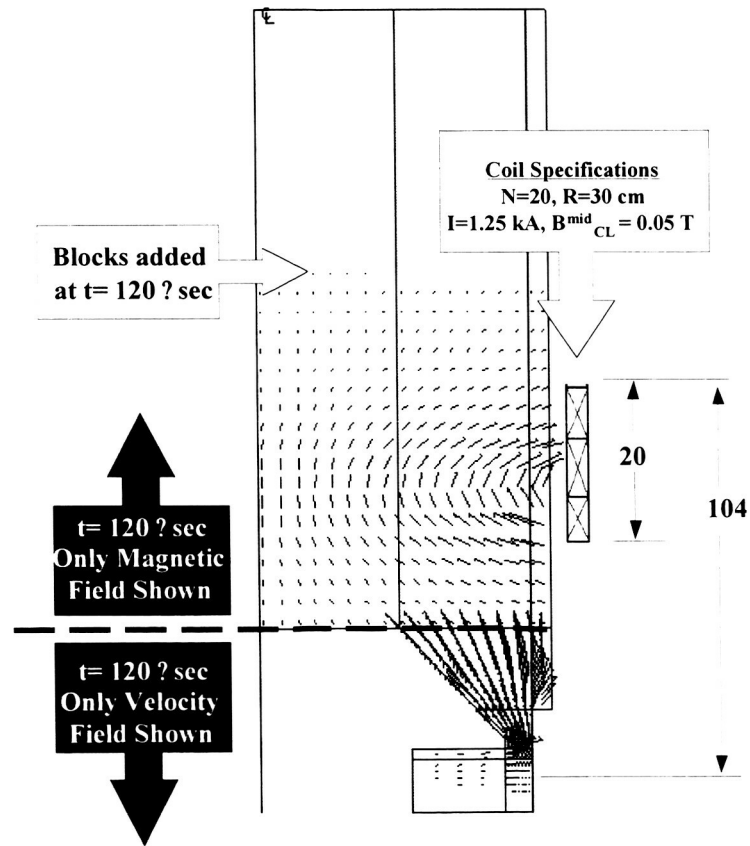


Figure 3-19. Geometry of case G-3 showing steady-state velocity field before adding the three blocks that carry the initial magnetic field distribution.

Figure 3-20 shows the evolution of pressure at the MPD gap. As in the simulations of section B.1 the history profile also exposes the times at which the compression waves reach the electrode gap. A comparison of conditions attained at the gap between the two cases however shows a peak plasma pressure that is about three times less for case G-3 than it is for case G-2. Moreover the wavelength of the pressure oscillations, shown in Figure 3-20, decreases with increasing time suggesting that the flow may reach steady-state by the end of the current pulse (~ 1-2 ms).

Fig 3-21 shows radial profiles of the axial velocity and Mach number attained at the gap at the time that the first compression wave reaches that location ($t=240 \mu\text{sec}$). The profiles show promise in that, even though the Mach number has decreased (due to the elevated temperatures associated with the compressed plasma at this location), the flow is still supersonic and the velocity is still in the order 60-100 km/sec. The temperature near the insulator surface is still high ($>10\text{eV}$) however, as shown in Fig 3-22, and therefore it is still a design concern.

At $t\sim 300 \mu\text{sec}$, the conditions are much more favorable. Fig 3-23 shows that the plasma temperature near the insulator is about an eV, with values in excess of 40 eV a few meters downstream of the electrodes – the intended stagnation region. Fig 3-24 confirms that the flow at the MPD gap is not choked. The pressure contours in Fig 3-23 (left) suggest that the flow is compressed along “slice location #1”, to below sonic conditions as shown in Fig 3-25 (right). The axial flow velocity remains high peaking at a value of 50 km/sec. Finally, Fig 3-26 shows that the flow remains subsonic downstream of “slice location #1”. “Slice location #3” is approximately 3 m downstream of the origin. Even though this arrangement has been able to achieve high temperatures and subsonic flow far beyond the magnet, the Mach number is still not low enough. Although we are about a factor of two away from reaching the desired plasma temperatures ($\sim 100 \text{ eV}$) we are still far from design pressure of $\sim 3 \text{ atm}$, as confirmed by Fig 3-26 left. That is because the flow is still high-speed at this location ($>50 \text{ km/sec}$). Once steady-state operation has been confirmed by extending the present simulation beyond 1 ms, future efforts must concentrate on relatively small changes in the magnet to accomplish additional compression of the flow thus extracting most of the kinetic energy still retained in the present set up.

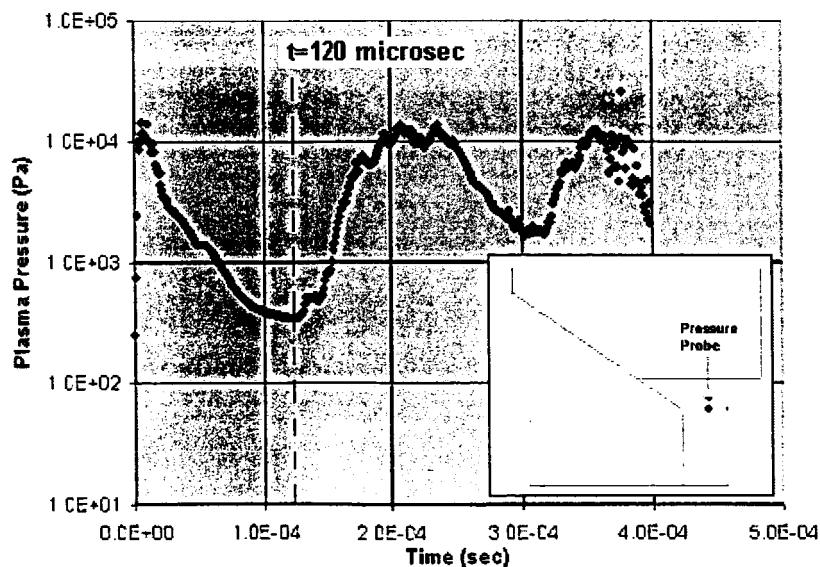


Figure 3-20. Pressure history at a point located midway through the electrode gap for case G-3.

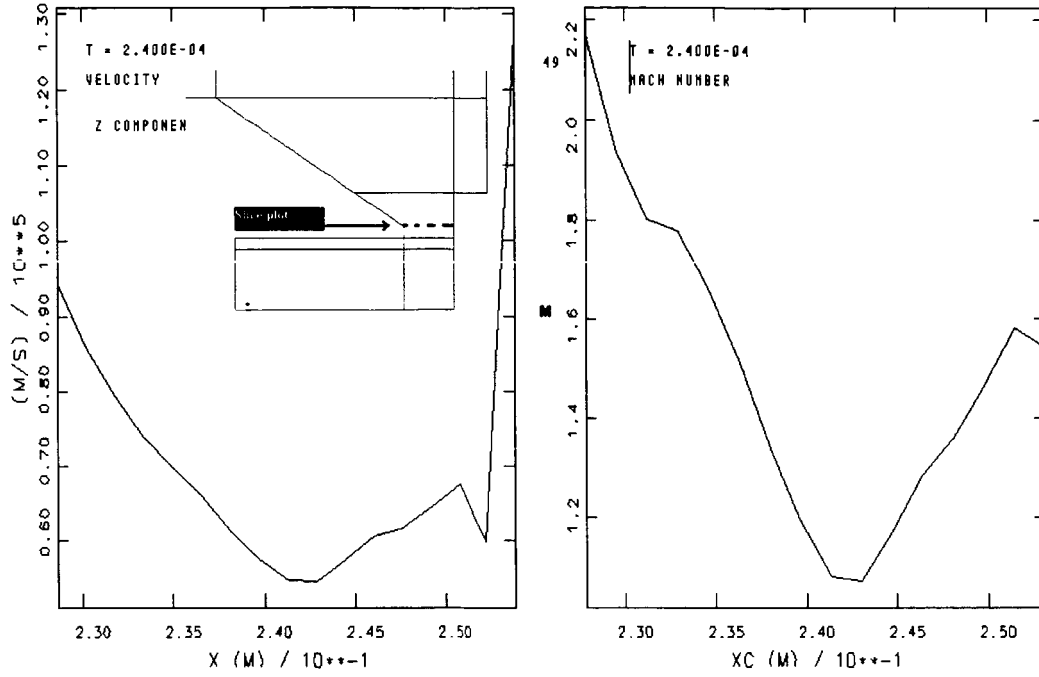


Fig 3-21. Radial profiles of axial velocity (left) and Mach no. (right) at the location shown on the left. (t=240 μ sec)

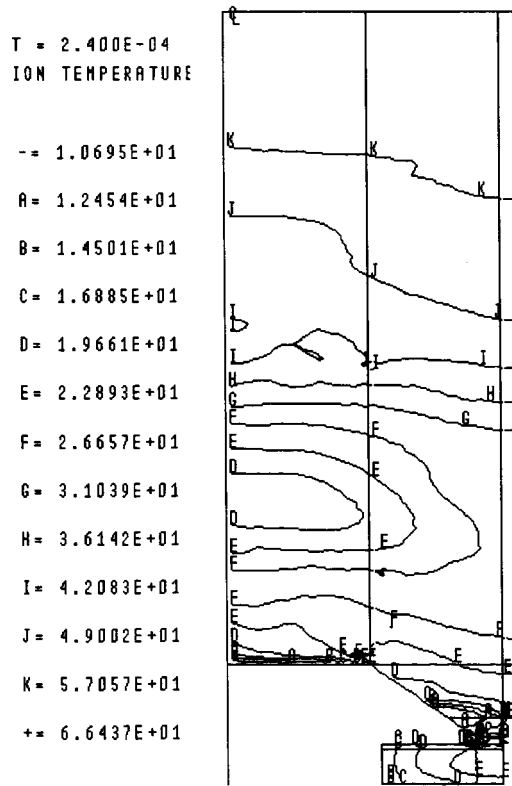


Fig 3-22. Ion temperature contours at $t = 240 \mu\text{sec}$.

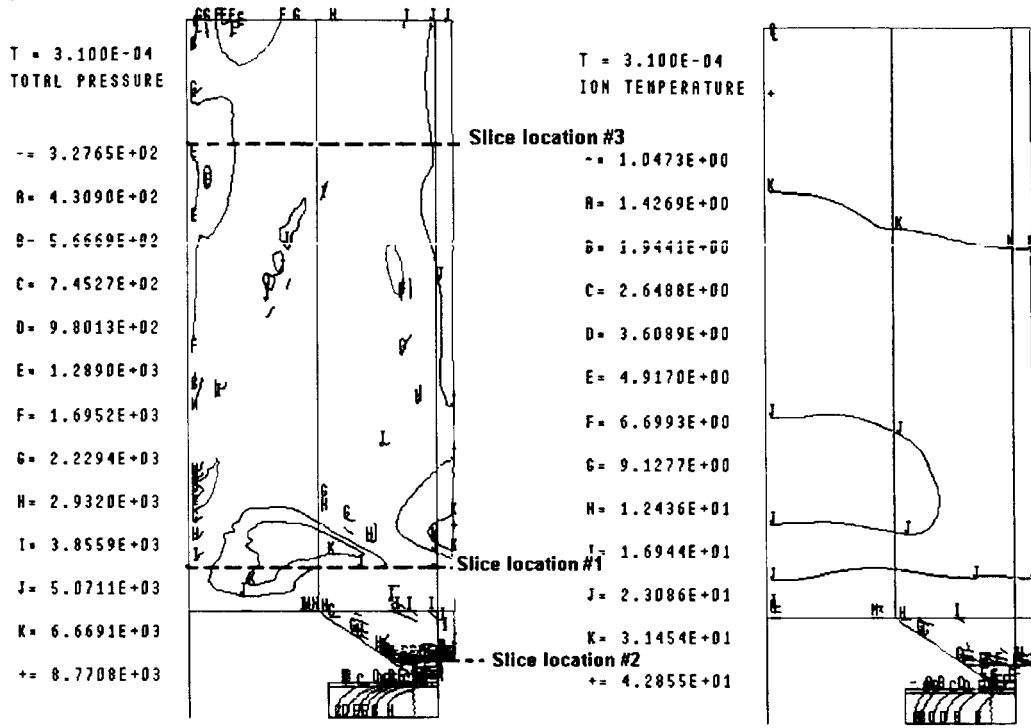


Fig 3-23. Pressure (left) and ion temperature (right) contours at $t = 310 \mu\text{sec}$.

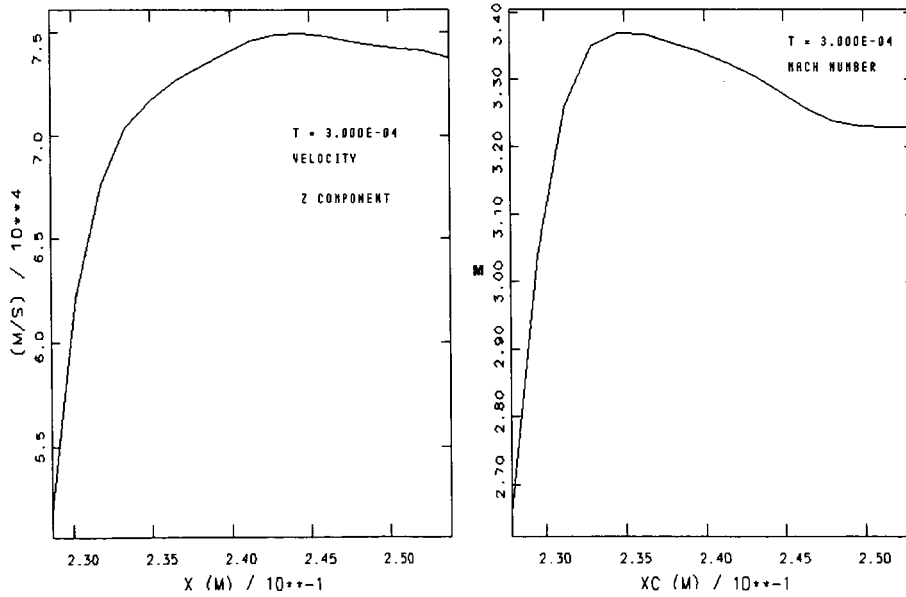


Fig 3-24. Radial profiles of axial velocity (left) and Mach no. (right) at slice location #2 ($t = 300 \mu\text{sec}$).

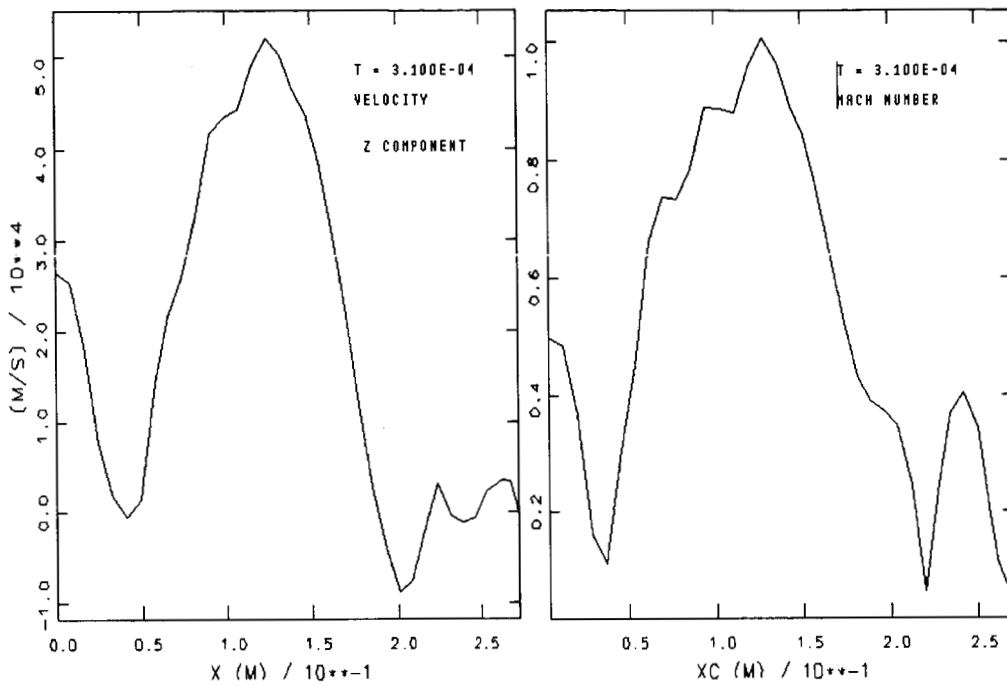


Fig 3-25. Radial profiles of axial velocity (left) and Mach no. (right) at slice location #1 ($t=310 \mu\text{sec}$)

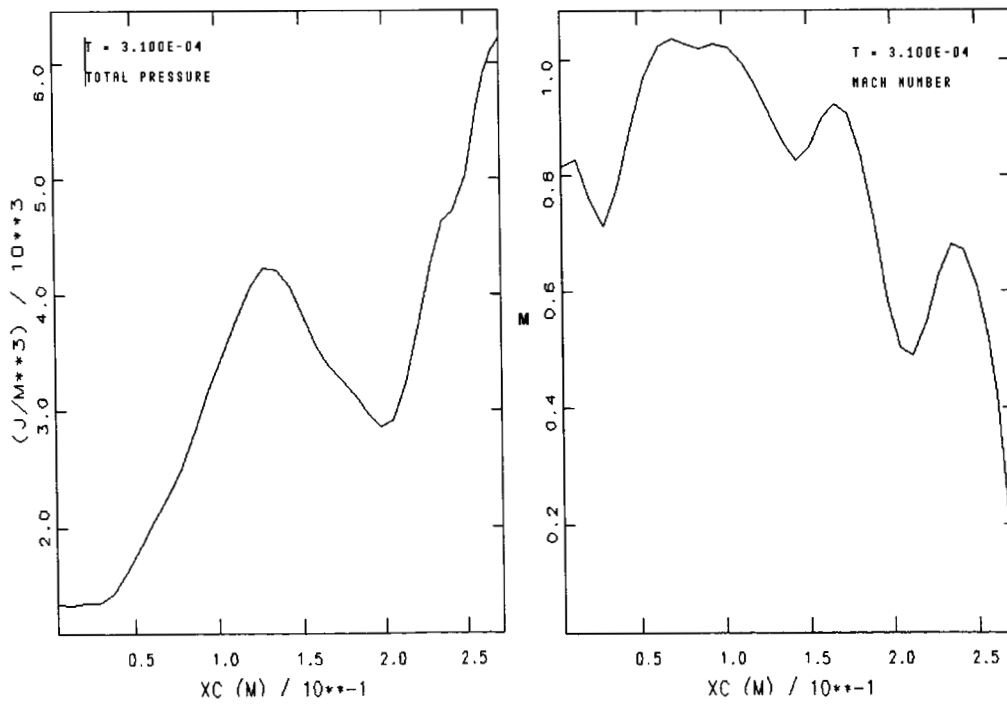


Fig 3-26. Radial profiles of plasma pressure (left) and Mach no. (right) at slice location #3 ($z = 3 \text{ m}$, $t = 310 \mu \text{ sec}$)

Magnetic Nozzle Conclusions

A number of geometrical configurations have been attempted in an effort to re-direct the flow farther downstream of the inner electrode. In the absence of the applied magnetic field, arrangement G-3 achieved more than 50 cm extension of the highest compression point on the centerline by comparison to the original geometry, G-0. With the magnet “turned on” after steady state flow had been achieved with geometry G-3, temperatures in excess of 50 eV are retained far downstream of the coil (>3 m). By comparison to previous efforts, the G-3 simulations are the first that accomplish such temperatures without choked flow at MPD gap. In summary the improvements attained in these most recent simulations compared to past work are as follow:

- High plasma temperatures (>40 eV) are sustained far downstream of the diffuser magnet
- Supersonic flow at MPD electrode gap survives the first compression waves induced by flow reflections off the applied magnetic field
- Pressure history at the electrode gap suggests that attainment of supersonic, steady state flow is possible

Future numerical simulation efforts should concentrate on:

- Confirmation that the desirable flow conditions at the MPD electrode are sustained for times much longer than a few hundred microseconds (→ prolong simulation)
- Further compression of plasma flow to extract more kinetic energy downstream of the magnet – present flow speeds remain too high (→ modify coil specifications in the current G-3 arrangement).

Conclusion

A combined experimental and theoretical effort has resulted in the design, construction, and operation of a 100 – MW class plasma source, and predictions of its operation in a downstream converging-diverging magnetic nozzle. The source has been operated at helium mass flow rates of .48, 6.45 and 27.8 g/s. These mass flow rates were determined both by calibration measurements and computational modeling of the flow from the propellant reservoir to the electrodes. Power levels up to 200 MW and currents up to 300 kA were used to accelerate these plasmas. Diagnostics of select firings of the source indicate downstream plasma densities on the order of 10^{14} m^{-3} and electron temperatures up to 15 eV. Data at 6.45 g/s indicate that the source was acting as a MPD accelerator, as it was designed for. At this operating point, voltage-current characteristics followed theoretical predictions spanning the full operating range from partially to fully ionized regimes. Results for higher mass flow rates indicate that the source did not achieve a fully ionized regime at the 27.8 g/s. Results at lower mass flow rates did not follow the trends predicted for MPD behavior; it is thought that the discharges at lower flow rates were not uniform.

The operation of the source with a downstream magnetic coil was examined theoretically and computationally. Two key results were obtained in this investigation. The first was that

timing of the downstream stagnation field with respect to initiation of the discharge is critical in allowing a smooth transition between the source and field, with no shocks. The second is that the current source, with an abrupt, 90° corner on the cathode at the exit, results in overexpansion and later pressure drops across oblique shocks. A more effective expansion was obtained in the model using an extended cathode with a 75° expansion angle. Temperatures on the order of 50 eV were predicted for the flow using the improved cathode design.

The work in this report has led to the capability of reliably operating a 300 MW MPD plasma source, and identified the possibilities and issues with increasing this power level up to 1 GW. Calculations have indicated the proper design and operation for this source with an external magnetic field to allow the experimental simulation of expanding fusion-edge-relevant plasmas in magnetic fields. A modified cathode, refined diagnostics and the design and installment of the stagnation coil would be required to carry this effort to its next level of understanding, and to a greater understanding of the expansion of fusion grade plasmas in magnetic nozzles. Diagnostic refinements to be considered would be improved triple probing methods to determine the density, temperature, and flow velocity of the plasma flow out of the source, and noninvasive spectroscopic techniques to address the flow through the applied magnetic fields.

References

- ¹ Turchi, P.J., "Design of a Gigawatt-Level, Quasi-Steady Flow Facility for Advanced Space Exploration Research," AIAA-1991-3613, AIAA/NASA/OAI Conference on Advanced SEI Technologies, Cleveland, Ohio, Sept. 1991.
- ² Marriott, D., *et al.*, "Performance of a MPD Plasma Source and Magnetic Nozzle for Fusion Propulsion," AIAA-2002-3934, 38th Joint Propulsion Conference and Exhibit, Indianapolis, Indiana, July 2002.
- ³ Mikellides, P.G., Turchi, P.J., and Mikellides, I.G., "Design of a Fusion Propulsion System, Part 1: Gigawatt-Level Magnetoplasmadynamic Source," *Journal of Propulsion and Power*, Vol. 18, No. 1, Jan. 2002.
- ⁴ Gilland, J. H., Kelly, A. J., and Jahn, R.G., "MPD Thruster Scaling," AIAA-87-0997, 19th International Electric Propulsion Conference, Colorado Springs, CO, May, 1987.
- ⁵ Lapointe, M., "High Power MPD Thruster Development at The NASA Glenn Research Center," IEPC-2003-0146, 28th International Electric Propulsion Conference, Toulouse, France, March 2003.
- ⁶ Choueiri, E. Y. *et al.*, "MPD Thruster Instability Studies," AIAA-87-1067, September 1987.
- ⁷ Jahn, R. G. *Physics of Electric Propulsion*, McGraw-Hill, New York, 1968, pp. 240-245.
- ⁸ Peterkin, R.E., Jr., and Frese, M.H., "MACH: A Reference Manual - First Edition," Air Force Research Laboratory: Phillips Research Site, 1998.
- ⁹ Mikellides, I.G., *et al.*, "Modeling of Magnetically-Guided Plasma Flows from a Gigawatt-Level Magnetoplasmadynamic Source," AIAA-2002-3934, 38th Joint Propulsion Conference and Exhibit, Indianapolis, Indiana, July 2002.